Monthly Notices of the ROYAL ASTRONOMICAL SOCIETY

MNRAS **445,** 3620–3649 (2014) doi:10.1093/mnras/stu1558

Hybrid methods in planetesimal dynamics: description of a new composite algorithm

P. Glaschke,[1★] P. Amaro-Seoane[2★] and R. Spurzem[1,3,4★]

[1]*Astronomisches Rechen-Institut, Mönchhofstraße 12-14, Zentrum für Astronomie, Universität Heidelberg, D-69120 Heidelberg, Germany*
[2]*Max Planck Institut für Gravitationsphysik (Albert-Einstein-Institut), D-14476 Potsdam, Germany*
[3]*National Astronomical Observatories of China, Chinese Academy of Sciences, 20A Datun Lu, Chaoyang District, 100012 Beijing, China*
[4]*Kavli Institute for Astronomy and Astrophysics, Peking University, 5 Yiheyuan Road, Haidian District, Beijing 100871, P. R. China*

Accepted 2014 July 30. Received 2014 July 24; in original form 2013 August 29

ABSTRACT

The formation and evolution of protoplanetary systems, the breeding grounds of planet formation, is a complex dynamical problem that involves many orders of magnitudes. To serve this purpose, we present a new hybrid algorithm that combines a Fokker–Planck approach with the advantages of a pure direct-summation *N*-body scheme, with a very accurate integration of close encounters for the orbital evolution of the larger bodies with a statistical model, envisaged to simulate the very large number of smaller planetesimals in the disc. Direct-summation techniques have been historically developed for the study of dense stellar systems such as open and globular clusters and, within some limits imposed by the number of stars, of galactic nuclei. The number of modifications to adapt direct-summation *N*-body techniques to planetary dynamics is not undemanding and requires modifications. These include the way close encounters are treated, as well as the selection process for the 'neighbour radius' of the particles and the extended Hermite scheme, used for the very first time in this work, as well as the implementation of a central potential, drag forces and the adjustment of the regularization treatment. For the statistical description of the planetesimal disc, we employ a Fokker–Planck approach. We include dynamical friction, high- and low-speed encounters, the role of distant encounters as well as gas and collisional damping and then generalize the model to inhomogenous discs. We then describe the combination of the two techniques to address the whole problem of planetesimal dynamics in a realistic way via a transition mass to integrate the evolution of the particles according to their masses.

Key words: methods: numerical – methods: statistical – planets and satellites: dynamical evolution and stability – protoplanetary discs.

1 INTRODUCTION

The formation of a planetary system is closely related to the formation of the host star itself. Cool molecular clouds collapse and fragment into smaller substructures which are the seeds for subsequent star formation. Angular momentum conservation in the forming clumps forces the infalling matter into a disc-like structure. The subsequent viscous evolution of the disc leads to a transport of angular momentum which channels gas to the protostar in the centre. These protoplanetary discs are the birth place of planets (for a detailed review see Armitage 2011). Embedded dust grains are the seed for the enormous growth to bodies of planetary size. The first hint to the structure of protoplanetary discs has been provided by our own Solar system. Through 'smearing out' all planets and adding the missing fraction of volatile elements, one can estimate the structure and mass of the protoplanetary disc. Since the efficiency of planet formation is unknown, this yields only a lower limit – the minimum-mass solar nebula (Hayashi 1981). The inferred surface density decreases with the distance from the sun as $\propto r^{-3/2}$.

Further insight has been obtained by the detection of an infrared excess of some stars, i.e. additional infrared radiation that does not originate from the star but an unresolved disc. Advancements in observation led in the mid-1990s to the direct imaging of nearby star-forming regions which opened a new flourishing field in astronomy (see O'dell, Wen & Hu 1993, for an example with *Hubble Space Telescope* images). Since then a big amount of observations of

★E-mail: Glaschke@ari.uni-heidelberg.de (PG); pau.amaro-seoane@aei.mpg.de (PA-S); spurzem@bao.ac.cn (RS)

© 2014 The Authors
Published by Oxford University Press on behalf of the Royal Astronomical Society

Downloaded from http://mnras.oxfordjournals.org/ at MPI Gravitational Physics on January 13, 2015

protoplanetary discs across the electromagnetic range has been obtained and interpreted, both space based (*ISO*, *Spitzer* and now *Herschel*) and in the ground [Very Large Telescope (VLT), VLT-I, Subaru, Keck]. We refer the reader to 'The Star Formation Newsletter' URL[1] for an overview of the recent papers in star and planet formation and the book review 'Protostars and Planets V' (Reipurth, Jewitt & Keil 2007).

Protoplanetary disc masses cover a range from 10^{-3} to $0.1\,\mathrm{M}_{\odot}$ with a peak around $0.01\,\mathrm{M}_{\odot}$ (data from Taurus/Ophiuchus; Beckwith 1996), and see Andrews et al. (2013) for Taurus–Auriga disc masses, in accordance with mass estimates deduced from the minimum-mass solar nebula. Since the disc lifetime cannot be measured directly, it is derived indirectly from the age of young, naked (i.e. discless) stars which sets an upper limit. Pre-main-sequence evolutionary tracks are used to gauge the stellar ages, providing lifetimes of a few 10^6 yr. The subsequent evolution of the disc proceeds in several stages.

Two different scenarios have been proposed to explain the formation of kilometre-sized planetesimals.

(i) One process is the gravitational instability of the dust component in a protoplanetary disc that leads to the direct formation of larger bodies. Goldreich & Ward (1973) propose that an initial growth phase of dust grains leads to a thin dust disc that undergoes a gravitational collapse. As the dense dust layer decouples from the gas, it rotates with the local Keplerian velocity, whereas the gas component rotates slower as it is partially pressure supported. This gives rise to a velocity shear at the boundary, which may excite turbulence through the Kelvin–Helmholtz instability. Since the motion of small dust grains in the boundary layer is coupled to the gas, the turbulent velocity field could suppress the formation of a stratified dust layer, which is a necessary prerequisite for the gravitational instability (Weidenschilling 1977).

(ii) The collisional agglomeration of dust particles is an opposed formation mechanism. Relative velocities are dominated by the Brownian motion in the early phases of the growth process. This mechanism becomes increasingly inefficient with growing mass, but successively the particles decouple from the gas and settle to the mid-plane – a process that yields even larger velocities with increasing mass. The sedimentation initiates a growth mode that is similar to the processes in rain clouds: larger grains drop faster, thus accreting smaller grains on their way to the mid-plane. Turbulence may modify this basic growth scenario by forcing the dust grains in a convection-like motion. Dust grains still grow during the settling process, but the turbulent velocity field could mix up dust from the mid-plane, and a new cycle begins. Each cycle adds a new layer to the dust grains – a mechanism that also operates in hail clouds – until the grains are large enough to decouple from the turbulent motion. Again, turbulence plays an important role in determining the growth mode and the relative velocities. While the relative velocities are high enough to allow for a fast growth, it is not clear a priori that collisions are sticky enough to allow for a net growth. High-speed encounters lead to fragmentation, which counteracts agglomeration (e.g. Blum & Wurm 2000, and references therein). An important bottleneck in the agglomeration process is the fast orbital decay of 1 m sized boulders. Their orbital lifetime is as short as 100 yr, and a quick increase in size – at least over one order of magnitude – is needed to reduce the radial drift significantly.

To overcome the difficulties associated with each of these scenarios, modifications have been proposed. Magnetohydrodynamic (MHD) simulations include electromagnetic interactions in hydrodynamical calculations. See the reviews of Balbus & Hawley 1998 and Balbus. 2003. The MHD simulations by Johansen, Klahr & Henning (2006) show that trapping of larger particles in turbulent vortices helps in increasing the orbital lifetime, but could also trigger local instabilities that may lead to the direct formation of planetesimals (Inaba et al. 2005). Johansen et al. (2007) describe a gravoturbulence mechanism as a feasible pathway to planetesimal formation in accreting circumstellar discs.

The details of agglomeration have drawn a lot of attention and are still under question (see Kempf, Pfalzner & Henning 1999; Paszun & Dominik 2009; Wada et al. 2009), but the successive agglomeration of planetesimals is commonly accepted.

In this paper, we present a hybrid algorithm that combines the advantages of a direct-summation code, NBODY6++, with a statistical one to treat the large number of bodies in the disc. The algorithm includes also a collisional and fragmentation model. NBODY6++ has been used to integrate dense stellar systems such as globular clusters and galactic nuclei, so that we need to modify it to suit the purpose of a long-term integration of planetesimals. On the other hand, a statistical approach allows us the integration of a very large number of bodies, but it must be able to treat the velocity dispersion consistently, deal with spatial inhomogeneities and include a wholly collision treatment. The limitation in both schemes is the *particle number*. In the case of the direct-summation code, on the large number, and in the case of the statistical one, on the low one. This means that NBODY6++ cannot integrate a realistically large number of particles as it would be needed and the statistical approach cannot give an accurate description of the evolution of the orbital elements of the bodies, because it treats the system as a continuum. We can combine the two approaches into a single one by addressing this issue with the introduction of a 'transition mass': low-mass particles are integrated with the statistical code and larger mass ones are treated with NBODY6++. A fiducial value for this mass is of about $3 \times 10^{-11}\ \mathrm{M}_{\odot}$.

In Section 2, we present the fundamentals of the theory of planet formation models that allows us to derive the initial models for the calculations, as well as a consideration about the orbits and protoplanet growth. In Section 3, we introduce the direct-summation integrator, as well as the required modifications for the specific problem of protoplanet formation. This had led to the so-called extended Hermite scheme, which is used for the first time here, the introduction of additional forces to treat correctly the dynamics of planetesimal discs, and the optimization of the integrator to the disc. In Section 4, we introduce the collisional and fragmentation algorithms, with the collisional cascades of Section 5 as a direct application of the fragmentation model. Size-dependent strength, the treatment of perturbations of equilibrium, migration and collisions, and the choice of a realistic collisional model are addressed in Sections 6, 7, 8, and 9, respectively. Section 10 presents and describes in detail the statistical model, and Section 11 finally explains the way we bring together the two approaches into a single code, the hybrid algorithm, which is the core of this paper. To finish with, in Section 12, we discuss our composite algorithm. All relevant tests, as well as the main results from the simulations are presented in Paper II, Amaro-Seoane et al. (2014), companion to this one.

[1] http://www.ifa.hawaii.edu/users/reipurth/newsletter.htm

Downloaded from http://mnras.oxfordjournals.org/ at MPI Gravitational Physics on January 13, 2015

2 INITIAL MODELS, ORBITS AND GROWTH

2.1 Initial models

The basis for all planet formation models is the structure of the protoplanetary disc. The work of Hayashi (1981) gives us a robust initial model. Subsequent evolution of the disc may change this simple approach, but it is still a valuable guideline.

The total surface density is estimated through the chemical composition of the disc, which gives the ratio of gas to solids. A fiducial value is 1:0.017 (see Cameron 1973). The surface density of the gas component is therefore (see Lodders 2003, and note metal abundance)

$$\Sigma_{\rm gas}(r) = 1700 \left(\frac{r}{1\,{\rm au}}\right)^{-3/2} {\rm g\,cm^{-2}}. \tag{1}$$

Since the dust content is rather low, the gaseous component is transparent to the visible solar radiation. Thus, the gas temperature follows from the radiation balance. The three-dimensional density structure is given by an isothermal profile with a radially changing scaleheight h. Since the density profile is related to a radially varying pressure, the gas velocity deviates from the local Keplerian velocity. The balance of forces relates the angular velocity $\Omega_{\rm g}$ to the pressure gradient and one can derive the angular velocity of the gas (Adachi, Hayashi & Nakazawa 1976). It is more appropriate to formulate the rotation of the gaseous disc in terms of a velocity lag $\Delta v_{\rm g}$ normalized to the local Keplerian velocity $v_{\rm K}$:

$$\begin{aligned}\Delta v_{\rm g} &= r(\Omega_{\rm g} - \Omega)\\ &\approx -\eta_{\rm g} v_{\rm K}.\end{aligned} \tag{2}$$

A typical value of $\Delta v_{\rm g}$ for the minimum-mass solar nebula at 1 au is $\Delta v_{\rm g} = -60\ {\rm m\,s^{-1}}$.

This simple model provides a brief description of the initial disc. However, the subsequent evolution further modifies the structure of the protoplanetary disc. Since embedded dust grains are coupled to the gas, it is likely that a global migration of solid material changes the surface density. Moreover, the dust grains are chemically processed, depending on the local temperature and composition which introduces additional spatial inhomogeneities. When the growing particles pass the critical size of ∼1 m, the strong onset of radial migration may lead to a final reshaping of the distribution of solid material. While these restrictions weaken the validity of this approach as the 'true' initial model, it is still a robust guideline to choose reasonable surface densities for the solid and the gaseous component after the formation of planetesimals.

2.2 Kepler orbits

Planetesimals in a protoplanetary disc are subjected to various perturbations: close encounters change their orbits, a small but steady gas drag gives rise to a radial drift and accretion changes the mass of the planetesimals. While all these processes drive the disc evolution on a time-scale of at least a few thousand years, each planetesimal moves most of the time on an orbit close to an unperturbed Kepler ellipse. Though the protoplanetary disc introduces additional perturbations, the central potential dominates for typical disc masses around 0.01 $M_\odot$. Therefore, the classical orbital elements still provide a proper framework to study planetesimal dynamics.

As long as no dominant body is structuring the protoplanetary disc, it is justified to assume axisymmetry. Hence, the argument of the perihelion ω, the longitude of the ascending node Ω and the eccentric anomaly $\phi_{\rm E}$ are omitted in the statistical description.

The deviation of planetesimal orbits from a circle is quite small. Thus, it is appropriate to expand the orbital elements of a test particle moving around a mass M: a planetesimal at a distance r_0, in a distance z above the mid-plane and with a velocity (v_r, v_ϕ, v_z) with respect to the local circular velocity $v_{\rm K}$ has orbital elements [leading order only, see Hornung, Pellat & Barge (1985) and check Goldreich & Tremaine (1978) for the origin of these ideas]:

$$a \approx r_0 + 2\frac{r_0 v_\phi}{v_{\rm K}} \tag{3}$$

$$e^2 \approx \frac{v_r^2 + 4v_\phi^2}{v_{\rm K}^2} \tag{4}$$

$$i^2 \approx \frac{z^2}{r_0^2} + \frac{v_z^2}{v_{\rm K}^2}, \tag{5}$$

where a is the semimajor axis, e is the eccentricity and i is the inclination of the orbit. These expressions allow us later a convenient transformation between the statistical representation through orbital elements and the utilization of a velocity distribution function.

2.3 Protoplanet growth

Our work follows the evolution of a planetesimal disc into few protoplanets, including the full set of interaction processes. Hence, we summarize the main aspects of protoplanet growth first to provide a robust framework.

During the initial phase, all planetesimals share the same velocity dispersion independently of their mass. The initial random velocities are low enough for an efficient gravitational focusing. Hence, the growth rate of a protoplanet with mass M and radius R can be estimated as (e.g. Ida, Kokubo & Makino 1993)

$$\dot{M} \approx v_{\rm rel}\frac{\Sigma}{H}\pi R^2\left(1 + \frac{2GM}{Rv_{\rm rel}^2}\right). \tag{6}$$

The scaleheight H (equation 165) and the relative velocity $v_{\rm rel}$ are related to the mean eccentricity $e_{\rm m} = \sqrt{\langle e^2\rangle}$ of the field planetesimals:

$$H \approx v_{\rm rel}/\Omega \qquad v_{\rm rel} \approx e_{\rm m} a\Omega. \tag{7}$$

Thus, the accretion rate in the limit of strong gravitational focusing ($2GM/R \gg v_{\rm rel}^2$) is

$$\dot{M} \approx 2\pi R\frac{\Sigma GM}{a^2\Omega e_{\rm m}^2} \tag{8}$$

$$\propto M^{4/3}. \tag{9}$$

The width Δa of this sphere of influence, the heating zone, is related to the Hill radius $R_{\rm Hill}$ of the protoplanet (Ida 1993):

$$\Delta a = \Delta\tilde{a} R_{\rm Hill} = 4R_{\rm Hill}\sqrt{\frac{4}{3}\left(\tilde{e}_{\rm m}^2 + \tilde{i}_{\rm m}^2\right) + 12}$$

$$h = \sqrt[3]{\frac{M}{3M_{\rm c}}}. \tag{10}$$

Here $\tilde{e}_{\rm m}$ and $\tilde{i}$ are eccentricity and inclination of the field planetesimals, scaled by the reduced Hill radius h of the protoplanet. $M_{\rm c}$ is the mass of the central star. The condition that the protoplanet controls the velocity dispersion of the field planetesimals reads (Ida et al. 1993)

$$\frac{2M^2}{2\pi a\Delta a} > \Sigma m. \tag{11}$$

Downloaded from http://mnras.oxfordjournals.org/ at MPI Gravitational Physics on January 13, 2015

This condition is equivalent to a lower limit of the protoplanetary mass:

$$\frac{M}{m} > \left(\frac{\pi\,\Delta\tilde{a}}{\sqrt[3]{3}}\right)^{3/5}\left(\frac{\Sigma a^2}{M_c}\right)^{3/5}\left(\frac{m}{M_c}\right)^{3/5}, \tag{12}$$

where M/m depends on several parameters, but reasonable values yield $M/m \approx 50$–100. The velocity dispersion in the heated region is roughly

$$v \approx R_{\rm Hill}\Omega, \tag{13}$$

which gives an interesting relation to the condition that leads to gap formation. A protoplanet can open a gap in the planetesimal component if it is larger than a critical mass $M_{\rm gap}$ (Rafikov 2001)

$$\frac{M_{\rm gap}}{M_c} \approx \begin{cases} \frac{\Sigma a^2}{M_c}\left(\frac{m}{M_c}\right)^{1/3} & \text{if } v \lesssim \Omega r_{\rm Hill} \\ \frac{\Sigma a^2}{M_c}\left(\frac{m}{M_c}\right)^{1/3}\left(\frac{\Omega r_{\rm Hill}}{v}\right)^2 & \text{if } v \gg \Omega r_{\rm Hill} \end{cases}, \tag{14}$$

where $r_{\rm Hill}$ is the Hill radius of the field planetesimals. The higher velocity dispersion of the field planetesimals (see equation 13) reduces the growth rate given by equation (8) to

$$\dot{M} \approx 6\pi\Sigma\Omega\frac{R R_{\rm Hill}}{\tilde{e}_{\rm m}^2} \tag{15}$$

$$\propto M^{2/3}. \tag{16}$$

Different mass accretion rates imply different growth mode. If two protoplanets have different masses M_1 and M_2, their mass ratio evolves as

$$\frac{\rm d}{{\rm d}t}\frac{M_2}{M_1} = \frac{M_2}{M_1}\left(\frac{\dot{M}_2}{M_2} - \frac{\dot{M}_1}{M_1}\right). \tag{17}$$

The field planetesimals also damp the excitation due to protoplanet–protoplanet interactions and keep them on nearly circular orbits. The balance between these scatterings and the dynamical friction due to smaller bodies establishes a roughly constant orbital separation b (Kokubo 1997):

$$b = R_{\rm Hill}\sqrt[5]{\frac{7\tilde{e}_{\rm m}^2 M}{2\pi\Sigma a R}} \tag{18}$$

$$\tilde{b} = b/R_{\rm Hill}, \tag{19}$$

where R is the radius of the protoplanet, M is its mass and $\tilde{e}$ is the reduced eccentricity of the field planetesimals. The stabilized spacing prevents collisions between protoplanets, but it also restricts the feeding zone – the area from which a protoplanet accretes. If all matter in the feeding zone is accreted by the protoplanet, it reaches its final isolation mass (Kokubo & Ida 2000):

$$M_{\rm iso} = 2\pi b a \Sigma. \tag{20}$$

Inserting equation (18) yields the isolation mass in units of the mass of the host star M_c:

$$M_{\rm iso}/M_c = (112\pi^4)^{3/8}\left(\frac{1}{3}\right)^{5/8}\left(\frac{4\pi}{3}\right)^{1/8}\left(\tilde{e}_{\rm m}^2\right)^{3/8} \times\left(\frac{a^2\Sigma}{M_c}\right)^{3/2}\left(\frac{a^3\rho}{M_c}\right)^{1/8} \approx 19.67\times\left(\tilde{e}_{\rm m}^2\right)^{3/8} \times\left(\frac{a^2\Sigma}{M_c}\right)^{3/2}\left(\frac{a^3\rho}{M_c}\right)^{1/8}. \tag{21}$$

In Table 1 we have values for the isolation mass for different surface densities. As the protoplanets approach the isolation mass, interactions with the gaseous disc and neighbouring protoplanets become increasingly important. We estimate the onset of orbit crossing by a comparison of the perturbation time-scale $\tau_{\rm pert}$ of protoplanet–protoplanet interactions with the damping time-scale $\tau_{\rm damp}$ due to planetesimal–protoplanet scatterings. Since the protoplanets are well separated ($\tilde{b} \approx 5\ldots10$), it is possible to apply perturbation theory (see e.g. Petit 1986):

Table 1. Isolation mass for different surface densities at $r = 1$ au and $M_c = 1\ {\rm M}_\odot$.

Σ(g cm^{-2})	$M_{\rm iso}/{\rm M}_\odot$	$M_{\rm iso}/{\rm M}_\oplus$
2	3.91×10^{-8}	0.013
10	4.33×10^{-7}	0.144
100	1.37×10^{-5}	4.548

$$\tau_{\rm pert} \approx \frac{\tilde{b}^5}{7\,h\Omega}. \tag{22}$$

We anticipate Section 10 to derive the damping time-scale

$$\tau_{\rm damp} \approx \frac{1}{2}\frac{T_{\rm r}^{3/2}}{\sqrt{2\pi}G^2\ln(\Lambda)(M+m)n_0\,m}, \tag{23}$$

where $T_{\rm r}$ and T_z are the radial and vertical velocity dispersion of the field planetesimals. Hence, the criterion for the onset of orbital crossing is

$$\tau_{\rm pert} < \tau_{\rm damp}. \tag{24}$$

As the protoplanets control the velocity dispersion of the field planetesimals (see equation 13), this condition reduces to

$$\Sigma_M > \Sigma_m\ln(\Lambda)\frac{72}{7\pi}\left(\frac{\tilde{b}}{\tilde{e}}\right)^4 > \Sigma_m\times f. \tag{25}$$

3 THE DIRECT-SUMMATION PART OF THE CODE

3.1 Direct *N*-body

The protoplanet formation is essentially an *N*-body problem. Although we seek for a more elaborated solution to this problem which benefits from statistical methods, the pure *N*-body approach is a logical starting point. Direct calculations with a few thousand bodies have provided us with a valuable insight into the growth mode (see e.g. Ida 1992; Kokubo 1996), but they are also powerful guidelines that help developing other techniques. Statistical calculations rely on a number of approximations and 'exact' *N*-body calculations provide the necessary, unbiased validation of the derived formula.

The choice of the integrator is a key element in the numerical solution of the equations of motion. Our requirements are the stable long-term integration of a few ten thousand planetesimals with the capability of treating close encounters, collisions and the perspective to evolve it into an improved hybrid code. Approximative methods like the Fast Multipole Method or Tree codes have a scaling of the computational time close to *N*, but the accuracy in this regime is too poor to guarantee the stable integration of Keplerian orbits (compare the discussion in Hernquist, Hut & Makino 1993; Spurzem 1999).

Downloaded from http://mnras.oxfordjournals.org/ at MPI Gravitational Physics on January 13, 2015

Taking all the requirements into account we have chosen NBODY6++[2], an integrator which is the most recent descendant from the famous *N*-body code family from S. Aarseths' 'factory'. This version was parallelized by Spurzem (1999), which opened the use of current supercomputers.

This parallel version, named NBODY6++, offers many versatile features that were included over the past years and more and more refined as time passed by. While all these elaborated tools deserve attention, we restrict ourselves for brevity to the components which contribute to the planetesimal problem. The main components of the code are as follows.

(i) Individual time steps and a block time step scheme.
(ii) Ahmad–Cohen neighbour scheme.
(iii) Hermite scheme.
(iv) KS-regularisation for close two-body encounters.

In section 2 of Paper II, we present a series of tests of the hybrid code, including obviously a check of the direct-summation *N*-body part of it. We successfully test the energy balance, we compare the cumulative size distribution, the mean square eccentricities and inclinations and the surface density and radial velocity dispersions.

3.2 Extended Hermite scheme

The Hermite scheme (Aarseth 1999, 2003) is an integral part of NBODY6++ and proved its value in many applications. It would have been natural to improve the performance with an additional iteration, but our first tentative implementations showed rather negative results: the iterated scheme was more unstable, slower and even less accurate than the plain Hermite scheme. An inspection of the code structure revealed that the Ahmad–Cohen neighbour scheme is the cause of this.

Each particle integration is composed of two parts – frequent neighbour force evaluations and less frequent total force evaluations including derivative corrections. Every regular correction leads to an additional change in the position of a particle, which introduces a spurious discontinuity in the neighbour force and its derivatives. The Hermite iteration reacts to this artificial jump in two ways: it increases the regular correction, and – what is more important – it amplifies any spurious error during the iteration which leads to an extreme unstable behaviour.

Since the Hermite iteration is a key element in the efficient integration of planetesimal orbits, we sought for a modification of the Hermite scheme that circumvents the depicted instability. The problem gives already an indication of a possible solution. A scheme with much smaller corrections would not suffer from the feedback of spurious errors.

NBODY6++ stores already the second and third time derivative of the forces for the time step calculation. A manifest application of these derivatives at hand is the improvement of the predictions to fourth order:

$$\boldsymbol{x}_p = \boldsymbol{x}_0 + \boldsymbol{v}_0\Delta t + \frac{1}{2}\boldsymbol{a}_0(\Delta t)^2 + \frac{1}{6}\dot{\boldsymbol{a}}_0(\Delta t)^3 + \frac{1}{24}\boldsymbol{a}_0^{(2)}(\Delta t)^4 + \frac{1}{120}\boldsymbol{a}_0^{(3)}(\Delta t)^5 \tag{26}$$

$$\boldsymbol{v}_p = \boldsymbol{v}_0 + \boldsymbol{a}_0\Delta t + \frac{1}{2}\dot{\boldsymbol{a}}_0(\Delta t)^2 + \frac{1}{6}\boldsymbol{a}_0^{(2)}(\Delta t)^3 + \frac{1}{24}\boldsymbol{a}_0^{(3)}(\Delta t)^4. \tag{27}$$

The prediction to fourth order was used in the iterative schemes of Kokubo, Yoshinaga & Makino (1998) and Mikkola & Aarseth (1998). Again, the new forces $\boldsymbol{a}_p$ and $\dot{\boldsymbol{a}}_p$ are calculated to improve $\boldsymbol{x}_p$ and $\boldsymbol{v}_p$ – but with a modified corrector:

$$\boldsymbol{a}_p = \boldsymbol{f}(\boldsymbol{x}_p, \boldsymbol{v}_p) \tag{28}$$

$$\dot{\boldsymbol{a}}_p = \boldsymbol{f}(\boldsymbol{x}_p, \boldsymbol{v}_p) \tag{29}$$

$$\boldsymbol{a}_n^{(2)}(t) = \frac{-4\dot{\boldsymbol{a}}_0 - 2\dot{\boldsymbol{a}}_p}{\Delta t} + \frac{-6\boldsymbol{a}_0 + 6\boldsymbol{a}_p}{\Delta t^2} \tag{30}$$

$$\boldsymbol{a}_n^{(3)}(t) = \frac{6\dot{\boldsymbol{a}}_0 + 6\dot{\boldsymbol{a}}_p}{\Delta t^2} + \frac{12\boldsymbol{a}_0 - 12\boldsymbol{a}_p}{\Delta t^3} \tag{31}$$

$$\boldsymbol{x}_c = \boldsymbol{x}_p + \frac{1}{24}(\boldsymbol{a}_n^{(2)} - \boldsymbol{a}_0{}^{(2)})(\Delta t)^4 + \frac{1}{120}(\boldsymbol{a}_n^{(3)} - \boldsymbol{a}_0{}^{(3)})(\Delta t)^5 \tag{32}$$

$$\boldsymbol{v}_c = \boldsymbol{v}_p + \frac{1}{6}(\boldsymbol{a}_n^{(2)} - \boldsymbol{a}_0{}^{(2)})(\Delta t)^3 + \frac{1}{24}(\boldsymbol{a}_n^{(3)} - \boldsymbol{a}_0{}^{(3)})(\Delta t)^4. \tag{33}$$

Finally, the derivatives are updated:

$$\boldsymbol{a}_0(t + \Delta t) = \boldsymbol{a}_p \tag{34}$$

$$\dot{\boldsymbol{a}}_0(t + \Delta t) = \dot{\boldsymbol{a}}_p \tag{35}$$

$$\boldsymbol{a}_0{}^{(2)}(t + \Delta t) = \boldsymbol{a}_n^{(2)} + \Delta t\, \boldsymbol{a}_n^{(3)} \tag{36}$$

$$\boldsymbol{a}_0{}^{(3)}(t + \Delta t) = \boldsymbol{a}_n^{(3)}. \tag{37}$$

Our new scheme has an appealing property, which is related to the usage of the higher force derivatives: as the predictor is fourth-order accurate, it is equivalent to one full Hermite step. Since the corrector uses new forces to improve the two highest orders, it is equivalent to a first iteration step. Thus, we obtained a one-fold iterated Hermite scheme at no extra cost. This extended Hermite scheme reduces the energy error by three orders of magnitude, compared to the plain NBODY6++ with the same number of force evaluations.

3.3 Additional forces for planetesimal disc dynamics

NBODY6++ only includes the gravitational interaction of all particles, therefore additional forces have to be added 'per hand'. A planetesimal disc requires two new forces: the presence of a central star introduces an additional central potential, while the gaseous component of the protoplanetary disc is the source of a friction force. It is important that the new forces are properly included in the neighbour scheme to assure that regular steps remain larger than irregular steps. Since a dissipative force breaks the energy conservation, one has to integrate the energy loss as well to maintain a valid energy error control. In the next subsections, we describe how we have done this.

[2] Aarseth (1999) gives a nice review on the remarkable history of the NBODY-codes, more details are given in Aarseth (2003).

Downloaded from http://mnras.oxfordjournals.org/ at MPI Gravitational Physics on January 13, 2015

3.3.1 Central potential

A star is much heavier than a planetesimal. Thus, the central star is introduced as a spatially fixed Keplerian potential:

$$\Phi_c = -\frac{GM_c}{r} \qquad \boldsymbol{F} = -\frac{GmM_c\,\boldsymbol{x}}{|\boldsymbol{x}|^3}. \tag{38}$$

Since the orbital motion of the planetesimals sets the dominant (and largest) dynamical time-scale in the system, we included the central force as a component of the regular force. Moreover, the central potential also introduces a strong synchronization, since planetesimals in a narrow ring share virtually the same regular block time step. Keeping the star spatially fixed is, in general, a valid approximation but, however, we note that for larger – but plausible – disc masses, of the order of 0.1 $M_\odot$, if a substantial fraction is incorporated into a massive planet, e.g. a 10 Jupiter-mass planet (rare, but known), then we would be running into a problem, because by holding fixed the star, the energy would alter other elements in the system, leading to instability. We refer the reader to Bromley & Kenyon (2006) for an example of code that allow the central star to move, and see Shu et al. (1990) for a general example of the issues involved in fixing the position of the star.

3.3.2 Drag force

As the whole planetesimal system is embedded in a dilute gaseous disc, each planetesimal is subjected to a small, but noticeable drag force. The drag regime[3] depends on the gas density and the size of the planetesimals. Kilometre-sized planetesimals are subjected to the deceleration

$$\frac{\mathrm{d}\boldsymbol{v}}{\mathrm{d}t} = -\frac{\pi C_D}{2m}\rho_{\rm gas}R^2|\boldsymbol{v}-\boldsymbol{v}_{\rm g}|(\boldsymbol{v}-\boldsymbol{v}_{\rm g}) \tag{39}$$

$$C_D = 0.5, \tag{40}$$

which is inversely proportional to the radius $R(m)$ of the planetesimal in this drag regime. $v_{\rm g}$ is the rotational velocity of the gaseous disc, which rotates slower than the planetesimal system as it is partially pressure supported. The drag force leads to an orbital decay $\dot{a}$ of the semimajor axis of a planetesimals:

$$\dot{a} = -\frac{3}{4}C_D\frac{\rho_{\rm gas}}{\rho_{\rm Body}}\frac{\langle(\Delta v)^2\rangle}{R(m)\Omega}. \tag{41}$$

Thus, smaller particles migrate faster, with a maximum at $R \approx 1$ m. Even smaller bodies couple to the gas, which reduces the effective drag force. The dissipation rate and its time derivative are

$$W_{\rm drag} = \boldsymbol{F}_{\rm drag}\cdot\boldsymbol{v}$$

$$\dot{W}_{\rm drag} = \dot{\boldsymbol{F}}_{\rm drag}\cdot\boldsymbol{v} + \boldsymbol{F}_{\rm drag}\cdot\boldsymbol{F}_{\rm tot}. \tag{42}$$

We integrate the dissipation rate $W_{\rm drag}$ to maintain a valid energy error:

$$\Delta E = \int_{t_1}^{t_2} W_{\rm drag}\,\mathrm{d}t \tag{43}$$

$$\Delta t = t_2 - t_1 \tag{44}$$

$$\Delta E = \frac{1}{2}\left(W_{\rm drag,1} + W_{\rm drag,2}\right)\Delta t + \frac{1}{12}\left(\dot{W}_{\rm drag,1} - \dot{W}_{\rm drag,2}\right)\Delta t^2 + \mathcal{O}(\Delta t^5). \tag{45}$$

The expression is fourth-order accurate in accordance with the order of the extended Hermite scheme. See Youdin & Chiang (2004) and Pinte & Laibe (2014) for examples of the application of the drag force.

3.3.3 Accurate integration of close encounters: tidal perturbations of KS-pairs and impact of the gaseous disc

Both new forces also demand a modification of the regularization treatment. They perturb the relative motion of a KS-pair and modify the orbit of the centre of mass. While the modification of the equations of motion is rather clear, the neighbour scheme requires some additional work.

Let $\boldsymbol{r}_1, \boldsymbol{r}_2$ be the positions of the two regularized particles. The equations of motion read ($G = 1$)

$$\boldsymbol{r} = \boldsymbol{r}_2 - \boldsymbol{r}_1$$

$$\ddot{\boldsymbol{r}}_1 = -M_c\frac{\boldsymbol{r}_1}{r_1^3} + m_2\frac{\boldsymbol{r}}{r^3} + \boldsymbol{F}_{\rm drag,1}$$

$$\ddot{\boldsymbol{r}}_2 = -M_c\frac{\boldsymbol{r}_2}{r_2^3} - m_1\frac{\boldsymbol{r}}{r^3} + \boldsymbol{F}_{\rm drag,2}, \tag{46}$$

where the perturbations by other particles have been omitted for clarity. Centre-of-mass motion and the orbital motion are separated:

$$\ddot{\boldsymbol{r}} = -M\frac{\boldsymbol{r}}{r^3} - M_c\frac{\boldsymbol{r}_2}{r_2^3} + M_c\frac{\boldsymbol{r}_1}{r_1^3} + \boldsymbol{F}_{\rm drag,2} - \boldsymbol{F}_{\rm drag,1} \tag{47}$$

$$\ddot{\boldsymbol{R}} = -M_c\frac{m_1}{M}\frac{\boldsymbol{r}_1}{r_1^3} - M_c\frac{m_2}{M}\frac{\boldsymbol{r}_2}{r_2^3} + \frac{m_1}{M}\boldsymbol{F}_{\rm drag,1} + \frac{m_2}{M}\boldsymbol{F}_{\rm drag,2} \tag{48}$$

$$\boldsymbol{r} = \boldsymbol{r}_2 - \boldsymbol{r}_1 \qquad M = m_1 + m_2 \tag{49}$$

$$\boldsymbol{R} = \frac{1}{M}(m_1\boldsymbol{r}_1 + m_2\boldsymbol{r}_2). \tag{50}$$

Two new contributions show up due to the external forces: the KS-pair is tidally perturbed by the central star and influenced by the gaseous disc. While the aerodynamic properties of a single particle are well understood, two bodies revolving about each other may induce complex gas flows in their vicinity, which could invalidate the linear combination of the drag forces on each component. Therefore, we drop the drag force term to avoid spurious dissipation. Since the dynamic environment allows virtually no stable binaries[4] in a planetesimal disc, the influence of the drag force on the encounter dynamics is negligible.

We further decompose the additional acceleration of the centre-of-mass motion, since the neighbour scheme benefits from a clear separation of the time-scales. Therefore, the tidal perturbation is

[3] The main drag regimes are Stokes (laminar flow), Epstein (mean free molecular path larger than object size) and Newton's drag law (turbulent flow). Weidenschilling (1977) provides a nice review on the different drag regimes.

[4] Tidal capturing of moons starts in the late stages of planet formation, but is limited to the planets or their precursors. However, the quiescent conditions in an early Kuiper belt lead to a more prominent role of binaries. See the summary of Astakhov, Lee & Farrelly (2005).

Downloaded from http://mnras.oxfordjournals.org/ at MPI Gravitational Physics on January 13, 2015

split into a smooth mean force and a perturbation force:

$$\ddot{\boldsymbol{R}} = \boldsymbol{F}_{\rm mean} + \boldsymbol{F}_{\rm pert}$$

$$\boldsymbol{F}_{\rm mean} = -M_{\rm c}\frac{\boldsymbol{R}}{R^3}$$

$$\boldsymbol{F}_{\rm pert} = M_{\rm c}\frac{\boldsymbol{R}}{R^3} - M_{\rm c}\frac{m_1}{M}\frac{\boldsymbol{r}_1}{r_1^3} - M_{\rm c}\frac{m_2}{M}\frac{\boldsymbol{r}_2}{r_2^3} \quad (51)$$

$$= 0 + \mathcal{O}(r^2). \quad (52)$$

The mean forces varies on the orbital time-scale and is hence included as a regular force component, while the perturbation is treated as an irregular force as it changes with the internal orbital period of the pair.

3.4 Further tuning the dial: optimizing *N*-body to the disc

An astrophysical simulation is a tool to analyse problems and predict dynamical systems which are not accessible to experiments. The design of a new simulation tool does not only require the careful implementation of the invoked physics, but also an analysis of the code performance to make best use of the available hardware.

We want to apply NBODY6++ for the first time to planet formation, a subject that is quite different to stellar clusters. The central star forces the planetesimals on regular orbits which need higher accuracy than the motion of stars in a cluster. In addition, the orbital motion also introduces a strong synchronization among the planetesimals, thus allowing a more efficient integration.

We examine the differences due to the integration of a disc system in the following sections. In particular, we will address in detail the role of the geometry of the problem and the neighbour scheme, the prediction of the number of neighbouring particles, the communication, the block size distribution and the optimal neighbour particle number for the direct summation of the massive particles in the protoplanetary system

3.4.1 Disc geometry and neighbour scheme

The introduction of the neighbour scheme by Ahmad & Cohen (1973) has provided us with a technique to save a considerable amount of computational time in star cluster simulations. Since the average ratio of the regular to the irregular time step $\gamma_{\rm t}$ is of the order of 10, the integration is speeded up by the same factor. One may expect a similar speedup for planetesimal systems, but in this case the time step ratio is roughly 3. The time step is calculated with the standard Aarseth time step criterion (it should be mentioned, however, that the relation of regular and irregular costs is more complicated with GPU technology)

$$\Delta t = \sqrt{\eta\frac{FF^{(2)} + (F^{(1)})^2}{F^{(1)}F^{(3)} + (F^{(2)})^2}}, \quad (53)$$

where $F^{(i)}$ are the force and its time derivatives. It is applied to the calculation of the regular step using the regular force and accordingly to the irregular step based on the irregular force. The regular time step of a particle orbiting the central mass $M_{\rm c}$ at a distance r_0 is

$$\Delta t_r = \sqrt{\eta_r}\frac{1}{\Omega} \qquad \Omega = \sqrt{\frac{GM_{\rm c}}{r_0^3}}. \quad (54)$$

For simplicity, we introduce the scaled time step ratio $\tilde{\gamma}_{\rm t} = \gamma_{\rm t}\sqrt{\eta_{\rm irr}/\eta_{\rm reg}}$. The free parameters of the problem are the mean

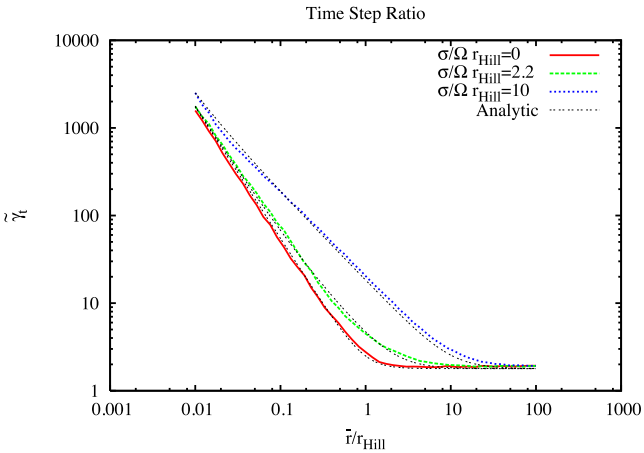

Figure 1. Time step ratio for $N_{\rm nb} = 100$. Curves are plotted for different values of $\sigma_{\rm v}/(r_{\rm Hill}\Omega)$. The dotted line is approximation (equation 59).

particle distance $\bar{r}$, the velocity dispersion $\sigma_{\rm v}$ (additional to the Keplerian shear), the particle mass m_i and the neighbour number $N_{\rm nb}$. We employ Hill's approximation for the central potential and obtain

$$\Delta t_i \approx \frac{\sqrt{\eta_i}}{\Omega} f(\Omega, r_{\rm Hill}, \bar{r}, \sigma_{\rm v}, N_{\rm nb}) \quad (55)$$

$$r_{\rm Hill} = r_0\sqrt[3]{\frac{2m_i}{3M_{\rm c}}}. \quad (56)$$

Here f is a yet unknown function. Dimensional analysis leads to

$$\Delta t_i \approx \frac{\sqrt{\eta_i}}{\Omega} f\left(\frac{\sigma_{\rm v}}{r_{\rm Hill}\Omega}, \frac{\bar{r}}{r_{\rm Hill}}, N_{\rm nb}\right) \quad (57)$$

$$\tilde{\gamma}_{\rm t} \approx f\left(\frac{\sigma_{\rm v}}{r_{\rm Hill}\Omega}, \frac{\bar{r}}{r_{\rm Hill}}, N_{\rm nb}\right) \quad (58)$$

which shows that the time step ratio is essentially controlled by the interparticle distance and the velocity dispersion. We generated different random realizations of planetesimals discs with different densities and velocity dispersions to cover the range of possible values. The neighbour number is fixed to $N_{\rm nb} = 100$ to reduce the noise due to small number statistics, but $\gamma_{\rm t}$ converges to a value independently of the neighbour number already for $N_{\rm nb} > 10$. Fig. 1 shows the numerical calculation of the time step ratio for various values of $\bar{r}$ and $\sigma_{\rm v}$. A good approximation to the calculated values of $\tilde{\gamma}_{\rm t}$ is

$$\tilde{\gamma}_{\rm t} \approx 1.79 \times \sqrt{1 + 1.03\frac{\sigma_{\rm v}^2}{\bar{r}^2\Omega^2} + 0.94\frac{r_{\rm Hill}^3}{\bar{r}^3}}. \quad (59)$$

Planetesimal discs have usually a small velocity dispersion (compared to the orbital velocity) and a low density in terms of the Hill radius, which leaves a major influence to the Keplerian shear. Since the shear motion is directly linked to the local Keplerian frequency, this synchronization reduces $\gamma_{\rm t}$ to values smaller than 10. The numerical calculations show larger time step ratios with increasing velocity dispersion and for high densities[5], but planetesimal discs are far from these extreme parameter values.

[5] $\bar{r}/r_{\rm Hill} < 1$ corresponds to an unstable self-gravitating disc.

Downloaded from http://mnras.oxfordjournals.org/ at MPI Gravitational Physics on January 13, 2015

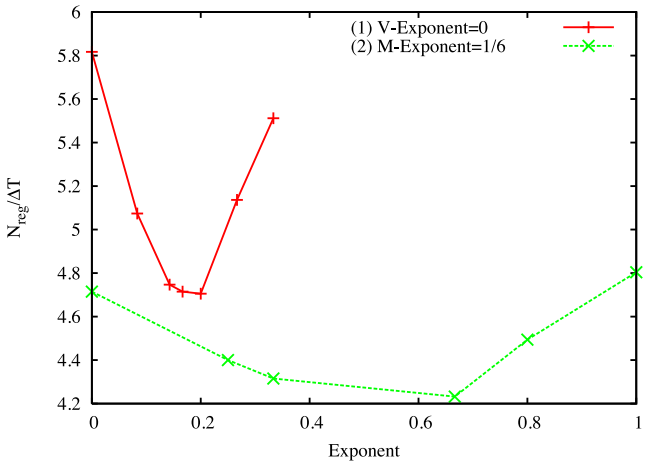

Figure 2. Regular steps per particle and per 1 N-body time in the inner core ($R_i < 0.5$) of a 5000 particle plummer model. Plotted are (1) different mass exponents with velocity exponent 0 and (2) different velocity exponents with mass exponent 1/6.

3.4.2 Optimal neighbour criterion

The standard neighbour criterion uses the geometrical distance: particles are neighbours if their distance to the reference particle is smaller than a limit R_s. This criterion is simple and probably the best choice for an equal-mass system. However, a multimass system may require a different criterion, since a massive particle outside the neighbour sphere could have a stronger influence than lighter particles inside the neighbour sphere. Also, relative effects are smaller at large distances. A more appropriate selection should rely on some 'perturbation strength' of a particle.

It turned out that a better criterion is the magnitude of the fourth time derivative of the pairwise force $F_{ij}^{(4)}$, i.e. those particles are selected as neighbours which produce the largest integration error in accordance with the Hermite scheme. $F_{ij}^{(4)}$ is a complicated expression (compare Appendix A), but the leading term can be estimated via dimensional analysis:

$$F_{ij}^{(4)} \propto \frac{m_j v_{ij}^4}{r_{ij}^6}. \tag{60}$$

We use this expression to define a new apparent distance between the integrated particle i and a neighbour j:

$$r_{\rm app} = r_{ij} \left(\frac{m_i}{m_j}\right)^{1/6} \left(\frac{v_{\rm s}}{v_{ij}}\right)^{2/3}, \tag{61}$$

where $v_{\rm s}$ is an arbitrary scaling velocity to obtain a distance with dimension length. This new distance definition moves massive or fast neighbours to an apparently smaller distance, thus enforcing that these particles are preferentially included in the neighbour list. In addition, the modified distance is readily included in the conventional neighbour scheme. We tested different mass and velocity exponents to verify that equation (61) is the optimal choice. Fig. 2 shows that these exponents are indeed the optimal choice for a Plummer model (Plummer 1911) with mass spectrum. The new scheme saves 25 per cent of the force evaluations in the core, but the impact on a planetesimals system is smaller, as it is the case for the neighbour scheme. While a velocity-dependent distance reduces the number of necessary full force evaluations, it introduces a distance changing with time which destabilizes the integration. The result is a much larger energy error compared to the achieved speedup. Therefore, we only recommend the mass modification of the apparent distance.

3.4.3 Neighbour changes

The rate at which the neighbours of a given particle change has a noticeable influence on the accuracy of the code. During the course of an integration, the second and third time derivative of the regular and irregular force are calculated from an interpolation formula. Whenever a particle leaves (or enters) the neighbour sphere, these derivatives are corrected by analytic expressions[6]. Hence, many neighbour changes lead to a pronounced spurious difference.

We estimated the rate at which particles cross the neighbour sphere boundary to quantify this effect. Neighbour changes are due to the Keplerian shear and the superimposed random velocities of the particles. The two effects lead to

$$\begin{aligned} N^{+/-} &= \Delta t_r \frac{N_{\rm nb}}{T_{\rm orb}} && \text{Shear} \\ N^{+/-} &= \frac{3}{2} \Delta t_r N_{\rm nb} \frac{\sigma_{\rm v}}{R_{\rm nb}} \\ &= \Delta t_r \frac{N_{\rm nb}}{T_{\rm orb}} \frac{3\pi\sigma_{\rm v}}{R_{\rm nb}\Omega} && \text{Dispersion,} \end{aligned} \tag{62}$$

where $R_{\rm nb}$ and $N_{\rm nb}$ are the neighbour sphere radius and the neighbour number, respectively. In practice, the neighbour changes due to the shear account for up to 80 per cent of the total neighbour changes. The standard regular time step $\Delta t_r = 2^{-5}$ and 50 neighbours yield a change of one particle per regular step, which is fairly safe.

3.4.4 Neighbour prediction

Each integration step is preceded by the prediction of all neighbours of the particles that are due. A regular step requires the full prediction of all particles, so there is no possibility to save computing time. In contrast, an irregular step calculates only neighbour forces, which requires the prediction of less particles. Thus, the prediction of all particles to prepare an irregular step is a simple, but, depending on the block size, computational costly solution. It seems to be more efficient to predict only the required particles, but random access to the particle data and the complete check of all neighbour list entries introduces an additional overhead. Therefore, large block sizes should favour the first approach, whereas the second approach is more suitable for small block sizes.

Both regimes are separated by a critical block size $N_{\rm irr}^*$. If $N_{\rm irr}$ particles with $\langle N_{\rm nb}\rangle$ neighbours are due, then only $N_{\rm merge}$ particles need to be predicted:

$$N_{\rm merge} \approx N_{\rm tot} \left(1 - \exp\left(-\frac{N_{\rm irr}\langle N_{\rm nb}\rangle}{N_{\rm tot}}\right)\right) \leq N_{\rm irr}\langle N_{\rm nb}\rangle. \tag{63}$$

The size $N_{\rm merge}$ of the merged neighbour lists is smaller than the total number of neighbour list entries, since some particles are by chance members of more than one neighbour list. Performance measurements show that the prediction of the merged neighbour lists is 10 per cent more costly (per particle) than the full prediction, mainly due to additional sorting and a random memory access. Thus $N_{\rm irr}^*$ satisfies

$$N_{\rm tot} = 1.1 \times N_{\rm merge}. \tag{64}$$

[6] Appendix A gives a complete set of the force derivatives up to third order.

Downloaded from http://mnras.oxfordjournals.org/ at MPI Gravitational Physics on January 13, 2015

Table 2. Ring Communication. Communication partners are fixed, while the exchanged data varies. $n_p - 1$ cycles are needed.

Process	0	1	2	3	4	5	6	7
Send to	1	2	3	4	5	6	7	0
Receive from	7	0	1	2	3	4	5	6

Table 3. Hierarchical Communication. Communication partners change after every cycle. The exchanged data amount doubles with every new cycle, hence only $\ln_2(n_p)$ cycles are needed.

Cycle	Process	0	1	2	3	4	5	6	7
1	Exchange with	1	0	3	2	5	4	7	6
2	Exchange with	2	3	0	1	6	7	4	5
3	Exchange with	4	5	6	7	0	1	2	3

Inserting equation (63) yields the critical block size:

$$N^*_{\rm irr} \approx 2.4 \frac{N_{\rm tot}}{\langle N_{\rm nb}\rangle}. \tag{65}$$

The prediction mode is chosen according to the actual block size.

3.4.5 Communication scheme

NBODY6++ is parallelized using a copy algorithm. A complete copy of the particle data is located on each node, so the integration step of one particle does not need any communication. Therefore, a block of $N_{\rm bl}$ particles is divided in n_p parts (n_p is the processor number), which are integrated by different processors in parallel. The integration step is completed by an all-to-all communication of the different subblocks to synchronize the particle data on all nodes. Hence, the amount of communicated data is proportional to $N_{\rm bl} \times n_p$. A communication in a ring-like fashion (see Table 2) needs $n_p - 1$ communication cycles, but a hierarchical scheme (see Table 3) sends the same amount of data with only $\ln_2(n_p)$ communication cycles. The difference between the two approaches remains small, as long as the communication is bandwidth limited, i.e. the blocks are large. Small block sizes shift the bottleneck to the latency, which is significantly reduced by the second scheme – especially if the code runs on many processors. See Table 5 for details on computers.

A hierarchical scheme reduces the latency, but nevertheless it is possible that the parallel integration is actually slower than a single CPU integration. We estimated both the runtime on one CPU and on a parallel machine to explore the transition between these two regimes. The latency time τ_l per communication is included in the wallclock time expressions for one regular/irregular step:

$$\tau_l = \alpha A$$

$$t_{\rm single} = \alpha N_{\rm bl} N_{\rm nb} \tag{66}$$

$$t_{\rm par} = \alpha \left(\underbrace{\frac{N_{\rm bl} N_{\rm nb}}{n_p}}_{\text{Arithmetic}} + \underbrace{A \ln_2(n_p)}_{\text{Latency}} + \underbrace{B N_{\rm bl}}_{\text{Communication}} \right). \tag{67}$$

If $t_{\rm single}$ (runtime on a single CPU) is equal to $t_{\rm par}$ (parallel computation), one can deduce the critical block size $N_{\rm min}$ which gives the minimal block size for efficient parallelization:

Table 4. Timings on a Beowulf cluster (Hydra, see Table 5). See text for an explanation of the variables. Timings are obtained for a maximal neighbour number LMAX=64. In practice, B is twice as large due to storage rearrangements in NBODY6++. See Appendix 5 for details on the computers.

Block	n_p	α(μs)	τ_l(μs)	A	B
Irregular	10	0.35	51	145	4.5
Regular	10	0.22	113	512	40
Irregular	20	0.35	308	877	8.8
Regular	20	0.22	368	1668	75

$$t_{\rm single} = t_{\rm par}$$

$$N_{\rm min} = \frac{A \ln_2(n_p) n_p}{N_{\rm nb}(n_p - 1) - B n_p}. \tag{68}$$

The hierarchical communication gives a minimal block size that increases logarithmically with the processor number. Equation (67) gives immediately the speedup S and the optimal processor number for a certain block size $N_{\rm bl}$:

$$S = \frac{n_p}{1 + A n_p \frac{\ln_2(n_p)}{N_{\rm bl} N_{\rm nb}} + B \frac{n_p}{N_{\rm nb}}}$$

$$n_{p,\rm opt}(N_{\rm bl}) = \frac{\ln(2) N_{\rm bl} \times N_{\rm nb}}{A} - \text{Hierarchical}. \tag{69}$$

A comparison to the optimal processor number for a ring communication

$$n_{p,\rm opt}(N_{\rm bl}) = \sqrt{\frac{N_{\rm bl} \times N_{\rm nb}}{A}} - \text{Ring}$$

$$t_{\rm par} = \alpha \left(\frac{N_{\rm bl} N_{\rm nb}}{n_p} + A n_p + B N_{\rm bl} \right) \tag{70}$$

stresses the efficiency of the hierarchical communication, since it allows a much larger processor number for a given problem size. Equations (66) and (67) are also useful to derive the total wallclock time, since the total runtime scales with the number of regular and irregular blocks:

$$N_{\rm reg} \approx T \frac{N^{1/3}}{N_{\rm nb}^{1/3} \sqrt{\eta_{\rm reg}}} \tag{71}$$

$$N_{\rm irr} \approx T \frac{N^{1/3}}{\sqrt{\eta_{\rm irr}}}. \tag{72}$$

These equations are only approximate expressions, but they give the right order of magnitude without detailed calculations that need a precise knowledge of the N-body model. Tables 4 and 6 summarize the timing parameters drawn from our experience with the Hydra and JUMP parallel supercomputers.

3.4.6 Block size distribution

The preceding section showed that the block size is closely related to the efficiency of the parallelization. Small blocks are dominated by the latency and the parallelization could be even slower than a single CPU calculation. Therefore, we derive the block size distribution for the block time step scheme to assess its influence on the efficiency.

Downloaded from http://mnras.oxfordjournals.org/ at MPI Gravitational Physics on January 13, 2015

Table 5. Specs of the different supercomputers used in running the algorithm.

Name	Beowulf (Hydra)	Titan	JUMP
Institute	ARI/ZAH	ARI/ZAH	Forschungszentrum Jülich
Location	Heidelberg	Heidelberg	Jülich
Processors	20	64	1248
Speed	2.2 GHz	3.2 GHz	1.7 GHz
Processors/Node	2	2	32
Network	Myrinet	Infiniband	Gigabit–Ethernet
Bandwidth	2 Gbit s^{-1}	20 Gbit s^{-1}	10 Gbit s^{-1}

Table 6. Timings on the IBM. More than 32 processors require more than one node.

Block	n_p	α(μs)	τ_l(μs)	A	B
Irregular	8	0.29	255	837	1.7
Regular	8	0.60	981	1763	4.1
Irregular	16	0.28	188	700	1.7
Regular	16	0.60	306	561	6.7
Irregular	64	0.27	241	887	7.7
Regular	64	0.46	401	871	21.7

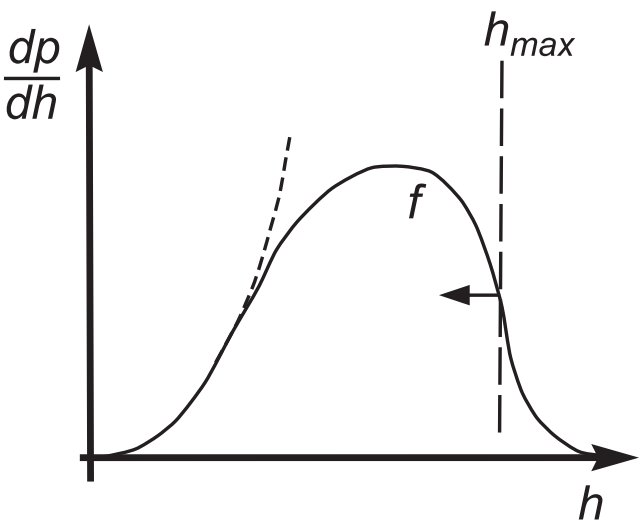

Figure 3. Time step distribution $f = \mathrm{d}p/\mathrm{d}h$. The short-dashed line on the left indicates approximation equation (74), whereas the dashed line on the right defines a reasonable upper limit $h_{\max}$.

Suppose that the time steps[7] h of all N particles in the model are distributed according to some known function f:

$$\mathrm{d}p = f(N, h)\,\mathrm{d}h, \tag{73}$$

where f is in most cases a complicated function. It involves spatial averaging and integration over the velocity distribution, which could be quite complicated even for simple time step formulae. Nevertheless, there is a constraint on the time step distribution, simply because every particle has a neighbour within a finite distance: there is some upper limit $h_{\max}$ that restricts the major fraction of the time steps to a finite interval. Thus, it is possible to capture the main features of the time step distribution with an expansion around $h = 0$ (Fig. 3 sketches this approximation):

$$f \approx C(N)h^a \qquad h \le h_{\max}, \tag{74}$$

where a is the lowest non-vanishing order of the expansion. Now, we consider a block level with the largest possible time step h_k. The number of particles $N_{\rm bl}$ in this block is

$$N_{\rm bl} = N \int_0^{h_k} f\,\mathrm{d}h \approx \frac{C(N)}{a+1}(h_k)^{a+1}. \tag{75}$$

According to the block time step scheme, the number of blocks per time with the largest possible time step h_k is proportional to $(h_k)^{-1}$. Therefore, the probability that a block size is in the range $[N_{\rm bl}, N_{\rm bl} + \mathrm{d}N_{\rm bl}]$ is

$$\mathrm{d}p \propto \sum_k \delta\left(N_{\rm bl} - \frac{C(N)}{a+1}h_k^{a+1}\right)\frac{1}{h_k}\mathrm{d}N_{\rm bl}, \tag{76}$$

where δ is Dirac's delta function. The sum over the logarithmically equidistant time steps h_k is approximated by an integral

$$\mathrm{d}p \propto \int_0^\infty \delta\left(N_{\rm bl} - \frac{C(N)}{a+1}h^{a+1}\right)\frac{\mathrm{d}\ln(h)}{h}\mathrm{d}N_{\rm bl}$$
$$\approx \frac{1}{a+1}N_{\rm bl}^{-(a+2)/(a+1)}\mathrm{d}N_{\rm bl}. \tag{77}$$

Thus, the average block size and the median of the block size distribution are

$$\langle N_{\rm bl}\rangle \approx \frac{1}{a}N^{a/(a+1)}$$
$$\mathrm{median}(N_{\rm bl}) \approx 2^{a+1}. \tag{78}$$

Special expressions for the average block size were already derived by Makino (1988), but the general relation of the time step distribution to the block size distribution is a new result. The median is surprisingly independent of the particle number, i.e. 50 per cent of all blocks are always smaller than a fixed value. It seems that this is a threat to the efficiency of the method, but the median of the wallclock time

$$\mathrm{median}(N_{\rm bl}^2) \approx \frac{N}{2^{(a+1)/a}} \tag{79}$$

demonstrates that these small blocks account only for a small fraction of the total CPU time. We confirmed the derived block size distribution (equation 77) by numerical calculations (see Fig. 4). The order parameter a is roughly two in (at least locally) homogenous systems, while an additional Keplerian potential reduces the order to $a = 1$. A planetesimal disc – or more precisely, a narrow ring of planetesimals – has a very narrow distribution of time steps since all particles share nearly the same orbital period. Thus, the regular block size is always equal to the total particle number making the parallelization very efficient.

[7] We use h instead of Δt in this section to avoid unclear notation.

Downloaded from http://mnras.oxfordjournals.org/ at MPI Gravitational Physics on January 13, 2015

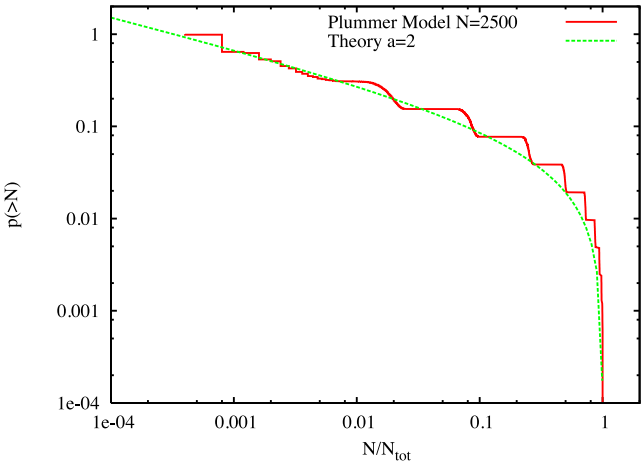

Figure 4. Cumulative irregular block size distribution for an $N = 2500$ particle Plummer model.

3.4.7 *Optimal neighbour number*

We treated the mean neighbour number $N_{\rm nb}$ so far as some fixed value. But it is also a mean to optimize the speed of the integration. Large neighbour spheres reduce fluctuations in the regular forces allowing larger regular steps, which reduces the total number of force evaluations. But larger neighbour lists also imply a larger communication overhead, as all the neighbour lists have to be broadcast to synchronize the different nodes. The best choice balances these two extremes, thus maximizing the speed.

Before we derive the optimal neighbour number on a parallel machine, we briefly summarize the known solution for a single CPU run (Makino 1988) for an extensive derivation. The computational effort of the irregular steps is proportional to the neighbour number, while the number of force evaluations for the regular steps is proportional to the total number of particles, reduced by the time step ratio $\gamma_{\rm t}$:

$$\gamma_{\rm t} := \frac{\Delta t_{\rm reg}}{\Delta t_{\rm irr}}$$

$$T_{\rm CPU} = f(N)\left(N_{\rm nb} + \frac{N}{\gamma_{\rm t}(N_{\rm nb})}\right) \tag{80}$$

$$\gamma_{\rm t}(N_{\rm nb}) \approx N_{\rm nb}^{1/3}, \tag{81}$$

where $f(N)$ collects all factors depending only on the total number of particles. Optimization with respect to the neighbour number $N_{\rm nb}$ yields the well-known result:

$$0 = \frac{\rm d}{{\rm d}N_{\rm nb}} T_{\rm CPU}$$

$$N_{\rm nb,opt} \propto N^{3/4}. \tag{82}$$

The calculation of the elapsed time for NBODY6++ on a PC cluster includes more terms. For clearness, we restrict ourselves to a rather simple model that involves only the dominant terms to show how parallelization influences the optimal neighbour number. We make the following approximations.

(i) We only take the force calculation and communication into account.

(ii) We use the same time constants for regular and irregular expressions.

(iii) We neglect all numerical factors that are comparable to unity.

The total CPU time is an extension of equation (70), which is applied to the regular and the irregular step. A new constant B_n includes the neighbour list communication separately, while all factors depending on N are represented by $f(N)$:

$$N_{\rm bl} \approx N^{2/3}$$

$$\gamma_{\rm t} \approx N_{\rm nb}^{1/3}$$

$$T_{\rm irr} = f(N)\left(\frac{N_{\rm bl}N_{\rm nb}}{p} + Ap + BN_{\rm bl}\right)$$

$$T_{\rm reg} = \frac{1}{\gamma_{\rm t}} f(N)\left(\frac{N_{\rm bl}N}{p} + Ap + (B + B_n N_{\rm nb})N_{\rm bl}\right)$$

$$T_{\rm tot} = T_{\rm irr} + T_{\rm reg}. \tag{83}$$

Optimization with respect to the processor number p leads to

$$0 = \frac{\partial}{\partial p} T_{\rm tot}$$

$$p_{\rm opt} = \sqrt{\frac{N^{2/3}N_{\rm nb}^{4/3} + N^{5/3}}{A(N_{\rm nb}^{1/3} + 1)}}$$

$$\approx \frac{N^{5/6}}{\sqrt{A}N_{\rm nb}^{1/6}}. \tag{84}$$

Further optimization with respect to the neighbour number gives the expression:

$$0 = \frac{\partial}{\partial N_{\rm nb}} T_{\rm tot} \tag{85}$$

$$0 = N_{\rm nb}^{4/3} - \frac{1}{3}N - \frac{1}{3}AN^{-2/3}p^2 - \frac{1}{3}Bp + \frac{2}{3}N_{\rm nb}B_n p. \tag{86}$$

For a fixed p or $B_n = 0$ (very fast neighbour list communication), we recover for large N:

$$N_{\rm nb,opt} \propto N^{3/4}. \tag{87}$$

In general, one cannot neglect the neighbour list communication. Therefore, we seek for the optimal choice of p and $N_{\rm nb}$, thus combining equations (84) and (86):

$$AN_{\rm nb}^{5/3} + \left(\frac{2}{3}N_{\rm nb} - \frac{B}{3B_n}\right)B_n\sqrt{A}N_{\rm nb}^{1/6}N^{5/6} = \frac{1}{3}(N_{\rm nb}^{1/3} + 1)NA. \tag{88}$$

Since this equation has no closed solution, we identify the dominant terms in equation (88) to calculate the asymptotic solution for large N:

$$N_{\rm nb,opt} \approx \left(\frac{A}{4B_n^2}\right)^{3/5} N^{1/5} \qquad N \gg \left(\frac{3A}{4B_n^2}\right)^{3/2}. \tag{89}$$

For small N, we get the approximated solution

$$N_{\rm nb,opt} \approx \left(\frac{N}{3}\right)^{3/5} \qquad N < \left(\frac{3A}{4B_n^2}\right)^{3/2}. \tag{90}$$

Fig. 5 compares the approximate expressions with the numerical solution of equation (88). In spite of the complicated structure of equation (88), both approximate expressions are reliable solutions.

Downloaded from http://mnras.oxfordjournals.org/ at MPI Gravitational Physics on January 13, 2015

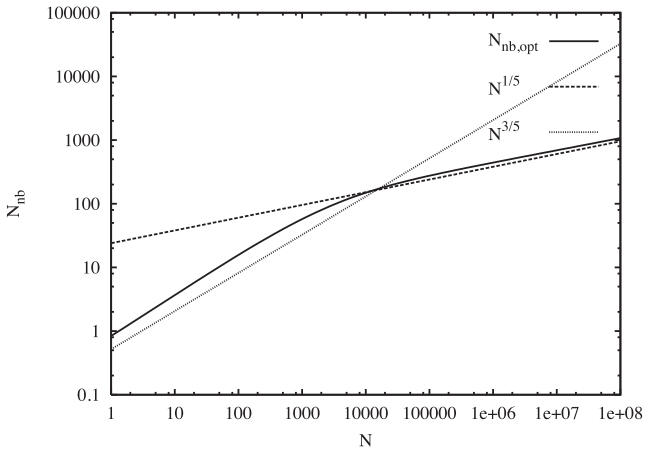

Figure 5. Optimal neighbour number as function of particle number N. The plot includes the numerical solution of equation (88) and the two asymptotic solutions. Timing constants are taken from a Beowulf cluster.

The example uses timing constants derived from our local Beowulf cluster:

$$A \approx 200 \quad B \approx 5 \quad B_n \approx 0.5. \tag{91}$$

If we compare the new optimal neighbour number to the single CPU expression (equation 82), we find that the influence of the neighbour list communication favours much smaller neighbour numbers. $N_{\rm nb}$ increases so slowly with the particle number that a neighbour number around 100 is a safe choice.

4 COLLISIONAL AND FRAGMENTATION MODEL

Some examples of fragmentation and accretion in the literature are Cazenave, Lago & Dominh (1982), Beauge & Aarseth (1990), Spaute et al. (1991), Wetherill & Stewart (1993) and Kenyon & Bromley (2004) for examples of coagulation as applied to planet formation. In our own algorithm, we use the approach of Glaschke (2003), which was applied to asteroid families. The following section describes the approach to fragmentation that is implemented in the code.

4.1 Handy quantities for quantifying the models

Although the whole scenario describing the process is quite complex, there are a few measures that describe the most important aspects.

(i) Mass of the largest fragment $M_{\rm L}$, or dimensionless $f_{\rm l} = M_{\rm L}/M$ where M is the combined mass of the two colliding bodies.
(ii) $f_{\rm l} < \frac{1}{2}$ refers to fragmentation, whereas $f_{\rm l} > \frac{1}{2}$ is denoted as cratering.
(iii) Energy per volume S that yields $f_{\rm l} = \frac{1}{2}$ is denoted as impact strength.
(iv) $f_{\rm KE} := 2E_{\rm kin}^{\rm frag}/E_{\rm kin}$: fraction of the impact energy that is converted into kinetic energy of the fragments.

Different fragment sizes and velocities are summarized by appropriate distribution functions. m_i, D_i and v_i are mass, diameter and modulus of the velocity of a given fragment, respectively.

(i) Fragment size distribution:

(a) $N_m(m)$: number of all fragments with a mass $m_i \geq m$,
(b) $M(m)$: mass of all fragments with a mass $m_i \geq m$,
(c) $N_D(D)$: number of all fragments with a diameter $D_i \geq D$.

The distribution functions are related to each other:

$$N_m(m) = N_D(D(m))$$

$$M(m) = \int_m^\infty x \left| \frac{{\rm d}N_m(x)}{{\rm d}x} \right| {\rm d}x$$

$$N_m(m) = \int_m^\infty \frac{1}{x} \left| \frac{{\rm d}M(x)}{{\rm d}x} \right| {\rm d}x.$$

$D(m)$ is the size–mass relation.

(ii) Velocity distribution:

(a) $\bar{v}(m)$: mean velocity as a function of mass.

4.2 Prediction of collisional outcomes: derivation from a Voronoy tessellation

Any theoretical or empirical prescription of a collision has to relate the aforementioned parameters, namely the impact energy, to the sizes and velocities of the produced fragments. The central quantity is the impact strength, which is a measure for the overall stability of a body. Objects smaller than 1 m are accessible to laboratory experiments, while collisions of larger bodies up to asteroid size have to be analysed by complex computer simulations. Asteroid families, which are remnants of giant collisions in the asteroid belt, provide independent insight, although the data is difficult to interpret.

We selected two different impact strength models as reference for our work. The first was obtained by Housen & Holsapple (1990) through the combination of asteroid family data and laboratory experiments via scaling laws:

$$S = S_0 \left(\frac{R}{1\,{\rm m}}\right)^{-0.24} \left[1 + 1.6612 \times 10^{-7} \left(\frac{R}{1\,{\rm m}}\right)^{1.89}\right]$$

$$f_{\rm KE} = 0.1 \tag{92}$$

$$S_0 = 1.726 \times 10^6\,{\rm J\,m^{-3}} = 1.726 \times 10^7 {\rm erg\,cm^{-3}}. \tag{93}$$

Later, Benz & Asphaug (1999) obtained another result through smoothed particle hydrodynamics simulations (for basalt, v =3 km s^{-1}):

$$S = S_0 \left(\frac{R}{1\,{\rm m}}\right)^{-0.38} \left[1 + 6.989 \times 10^{-5} \left(\frac{R}{1\,{\rm m}}\right)^{1.74}\right]$$

$$f_{\rm KE} \approx 0.01 \tag{94}$$

$$S_0 = 6.082 \times 10^5\,{\rm J\,m^{-3}} \tag{95}$$

$$\rho = 2.7\,{\rm g\,cm^{-3}}. \tag{96}$$

$f_{\rm KE}$ is a measure of the kinetic energy that is transferred to the fragments:

$$E_{\rm kin}^{\rm frag} = \frac{f_{\rm KE}}{2} E_{\rm kin}. \tag{97}$$

See Fig. 7 for a depiction, we introduce a dimensionless measure γ of the relative importance of gravity for the result of a collision. It

Downloaded from http://mnras.oxfordjournals.org/ at MPI Gravitational Physics on January 13, 2015

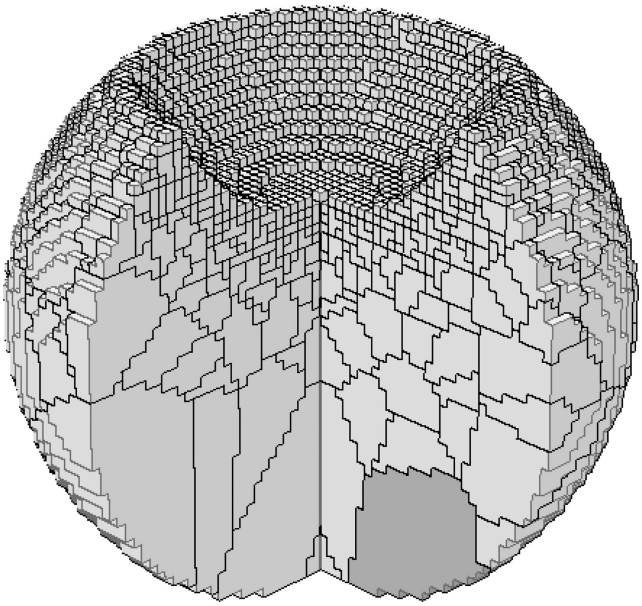

Figure 6. Section for $f_1 = 0.04$ and $n = 3$. The largest fragment is coloured in dark grey. In this calculation, $60 \times 60 \times 60$ grid cells are used. Note the decomposition in grid cells and the Voronoy polyhedra which form the fragments.

is defined as the ratio of the energy per volume S_G that is necessary to disperse the fragments to the impact strength S_0:

$$S_G = 2\pi \frac{4 - 2\sqrt[3]{2}}{5 f_{\mathrm{KE}}} G R^2 \rho^2$$

$$\gamma := S_G / S. \tag{98}$$

The first step towards the prediction of a collisional outcome is to relate the impact energy and the impact strength to ascertain the size of the largest fragment f_1. Laboratory experiments and simulations indicate the functional form

$$\epsilon(f_1) = \begin{cases} 2(1 - f_1) & \text{for} \quad f_1 > \frac{1}{2} \\ (2 f_1)^{-\frac{1}{K}} & \text{otherwise} \end{cases}.$$

$$\epsilon = \frac{E_{\mathrm{kin}} \rho}{2SM}, \tag{99}$$

which is both valid in the fragmentation regime and the cratering limit. The size of the largest fragment is used to derive the full size distribution. To accomplish the decomposition 'seed fragments' are distributed inside the target according to the largest desired fragment. The full set of fragment is derived from a Voronoy tessellation[8] using these seed points. Fig. 6 depicts the result of such a decomposition. The fragment velocities are calculated from the total kinetic energy after the collision to initiate a post-collisional N-body calculation to treat reaccumulation.

We conducted a large set of such calculations to cover a sufficient range in f_1^i (i.e. impact energy) and γ (i.e. body size). Table 7 summarizes the derived values of the largest and second largest fragment including reaccumulation. For the strength of planetesimals and large objects, see Leinhardt & Stewart (2012).

[8] The Voronoy tessellation assigns every volume element to the closest seed point. First applications date back to the 17th century, but the Russian mathematician of Ukrainian origin Georgy Feodosevich Voronoy put it on a general base in 1908.

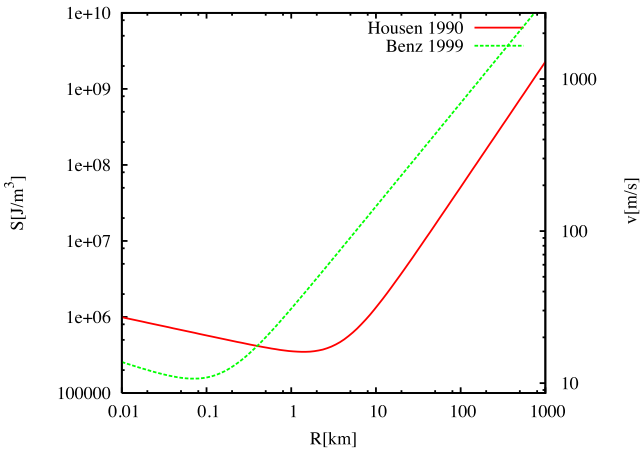

Figure 7. Impact strength according to equations (92) and (94). The right axis gives the corresponding impact velocity according to $S = 1/2\rho v^2$ with $\rho = 2.7\ \mathrm{g\,cm^{-3}}$.

We note that the connection to the collision energy needed to fragment an object and eject half of the mass of the combined pair to infinity, usually referred to as Q, is that this quantity is the total energy, and S the energy per volume.

5 COLLISIONAL CASCADES

Although the formation of planets requires a net growth due to collisions, this destructive process plays a role in the formation of larger bodies as the overall size distribution controls the accretion rate of the protoplanets. While this has been addressed in detail by Kobayashi et al. (2010) and Belyaev & Rafikov (2011), we deem it worth to have a closer look into this mechanism now within our approach.

5.1 Self-similar collisions

The first step is to decompose an inhomogeneous system into smaller subvolumes which are locally homogenous. Furthermore, it is assumed that these subvolumes hardly interact with each other. Hence, it is possible to apply the *particle-in-a-box-method* (Safronov 1972) to analyse collisions within the small subvolumes.

The distribution function is evolved by the coagulation equation. We modified the equation given by Tanaka, Inaba & Nakazawa (1996) by introducing a new function M_{red} to arrive at a more concise expression:

$$0 = \frac{\partial}{\partial t} m n(t, m) + \frac{\partial}{\partial m} F_{\mathrm{m}}(t, m), \tag{100}$$

where $n(m)$ is the distribution function. The mass flux F_{m} is given by

$$F_{\mathrm{m}} = -\int\int n(t, m_1) n(t, m_2) \xi \, \mathrm{d}m_1 \mathrm{d}m_2$$

$$\xi \equiv \sigma(m_1, m_2) v_{\mathrm{rel}} M_{\mathrm{red}}(m, m_1, m_2) \tag{101}$$

$$M_{\mathrm{tot}} = \int n(t, m) m \mathrm{d}m \tag{102}$$

$$\frac{\partial}{\partial t} M_{\mathrm{tot}} = F_{\mathrm{m}}(m_{\mathrm{min}}), \tag{103}$$

where ξ is the coagulation kernel, n is the already introduced size distribution, v_{rel} is the mean relative velocity, σ is the cross-section for colliding bodies (m_1, m_2) and M_{red} is the newly introduced

Downloaded from http://mnras.oxfordjournals.org/ at MPI Gravitational Physics on January 13, 2015

Table 7. Data compilation of the fragmentation calculations.

γ f_1^i	0.1	0.2	0.3	0.4	0.5	0.6	0.7	0.8
				Largest fragment				
0.025 52	0.100 00	0.200 00	0.300 00	0.400 00	0.500 00	0.600 00	0.700 00	0.800 00
0.198 97	0.100 00	0.200 00	0.300 00	0.400 00	0.500 00	0.600 00	0.700 00	0.800 00
0.679 85	0.100 00	0.200 00	0.300 00	0.400 00	0.576 12	0.673 15	0.820 06	0.960 73
1.140 50	0.100 00	0.315 26	0.357 08	0.613 62	0.835 11	0.928 32	0.943 80	0.975 72
1.770 57	0.108 84	0.588 83	0.759 74	0.879 22	0.927 55	0.936 62	0.971 07	0.979 24
2.260 21	0.158 95	0.688 91	0.872 17	0.895 92	0.929 65	0.960 89	0.967 01	0.987 27
3.116 26	0.309 54	0.837 74	0.902 72	0.926 82	0.959 43	0.955 65	0.976 77	0.987 91
				Second largest fragment				
0.025 52	0.081 71	0.107 70	0.064 71	0.081 07	0.049 76	0.039 82	0.031 71	0.021 55
0.198 97	0.091 74	0.095 33	0.084 10	0.069 67	0.049 30	0.048 25	0.035 10	0.020 77
0.679 85	0.077 13	0.083 65	0.077 91	0.083 87	0.070 26	0.061 47	0.060 82	0.008 47
1.140 50	0.086 21	0.072 56	0.103 31	0.096 40	0.024 67	0.006 75	0.007 83	0.002 65
1.770 57	0.079 09	0.055 49	0.069 61	0.020 35	0.003 29	0.007 19	0.002 73	0.001 61
2.260 21	0.066 93	0.022 88	0.005 28	0.008 82	0.005 84	0.002 68	0.006 64	0.001 26
3.116 26	0.069 40	0.008 84	0.003 84	0.004 88	0.000 64	0.010 07	0.002 25	0.001 62

fragment redistribution function. $M_{\rm red}$ contains all information on the fragments arising from the breakup of body m_1 due to the impact of body m_2. Its definition avoids double counting of collisions in the above integral. The redistribution function is related to the differential number distribution function $n_{\rm coll}(m_1, m_2, m)$, i.e. the number of fragments produced by a collision per mass interval. Since the target m_1 formally disappears, it is included as a negative contribution:

$$M_{\rm red}(m, m_1, m_2) := \int_0^m \Big(n_{\rm coll}(m_1, m_2, \tilde{m}) - \delta(\tilde{m} - m_1)\Big)\tilde{m}\,{\rm d}\tilde{m}. \tag{104}$$

Mass conservation in each collision is reflected by $M_{\rm red}(0, m_1, m_2) = M_{\rm red}(\infty, m_1, m_2) = 0$. The cross-section σ depends on the velocities and radii R_i of the particles. A simple approach is the geometric cross-section:

$$\sigma(m_1, m_2) = \pi(R_1 + R_2)^2. \tag{105}$$

If gravity plays an important role during encounters, we have to take into account gravitational focusing:

$$\sigma(m_1, m_2) = \pi(R_1 + R_2)^2 \left[1 + \frac{2G(m_1 + m_2)}{v_{\rm rel}^2(R_1 + R_2)}\right]. \tag{106}$$

A special class of collisional models are self-similar collisions. Self-similarity implies an invariance of the collisional outcome with respect to the scale of the colliding bodies. If the target mass as well as the projectile mass are enlarged by a factor of 2, then only the masses of all fragments doubles without further changes in the collisional outcome. They allow us to introduce the convenient dimensionless fragment redistribution function f_m:

$$M_{\rm red}(m, m_1, m_2) = m f_m(m_1/m, m_2/m). \tag{107}$$

We follow Tanaka et al. (1996) and employ the substitution[9] $m_1 = mx_1$, $m_2 = mx_2$ to simplify equation (101):

$$F_m = -\iint n(t, mx_1)n(t, mx_2)m^{11/3} \times \sigma(x_1, x_2)v_{\rm rel} f_m(x_1, x_2)\,{\rm d}x_1\,{\rm d}x_2. \tag{108}$$

[9] A similar approach to the solution of the coagulation equation is the Zakharov transformation, see Connaughton, Rajesh & Zaboronski (2004).

A simple solution is a steady-state cascade with F_m = const. The loss of bodies of a given size is balanced by the fragment supply from larger bodies, hence the system maintains a steady state $\frac{\partial}{\partial t}n(t, m) = 0$. Equation (108) inspires the ansatz $n(m) \propto m^{-k}$, which yields $k = 11/6$. This is the well-known equilibrium slope in self-similar collisional cascades, which was already found by Dohnanyi (1969). Strong gravitational focusing changes the exponent[10] to $k = 13/6$. Both steady-state solutions seem to be rather artificial, as they contain an infinite amount of mass and require a steady mass influx from infinity. However, they provide an appropriate description for the relaxed fragment tail of a size distribution, as long as the largest bodies provide a sufficient flux of new fragments. Once the largest bodies start to decay, the finite amount of mass in the system leads to an overall decay of the collisional cascade. Thus, we seek for a more general solution to equation (100) using the ansatz $n(t, m) = a(t)n_0(m)$:

$$\frac{\partial}{\partial t}a(t) = -Ca(t)^2 \tag{109}$$

$$mn_0(m) = \frac{1}{C}\frac{\partial}{\partial m}F_m, \tag{110}$$

where C is determined by fixing n_0 at an arbitrary value m^*. $a(t)$ is independent of the collision model:

$$a(t) = \frac{1}{1 + Ct} \tag{111}$$

$$C \propto n(m^*). \tag{112}$$

A power-law solution is $n_0(m) \propto -Cm^{-k+1}$ which is only valid for $C < 0$ (agglomeration dominates). To examine $C > 0$, we perturb the already known equilibrium solution:

$$n_0(m) = N_0\, m^{-k} - CN_1\, m^{-2k+2} + \mathcal{O}(C^2) \tag{113}$$

$$\frac{1}{N_1} = (2 - k)\iint x_1^{-k}x_2^{-2k+2}\sigma(x_1, x_2) \times v_{\rm rel}\,(f_m(x_1, x_2) + f_m(x_2, x_1))\,{\rm d}x_1{\rm d}x_2, \tag{114}$$

[10] Tanaka et al. (1996) state that $k < 2$ is a necessary condition for a finite mass flux. However, their analysis is not valid for all possible collisional models.

Downloaded from http://mnras.oxfordjournals.org/ at MPI Gravitational Physics on January 13, 2015

where N_1 is small if the integral on the right-hand side is large. This is the case for a sufficiently large impact strength. Equation (113) has the interesting property that $n(m') = 0$ for some mass m', given that $k < 2$. This mass m' represents the largest body in the system, e. g. the largest asteroid in a fictitious asteroid belt.

6 SIZE-DEPENDENT STRENGTH

We model the size-dependent strength S with a power law to examine the influence on the equilibrium solution. The velocity dispersion v and the collisional cross-section σ are also modelled with power laws to account for relaxation processes:

$$v = v_0 \left(\frac{m}{m_0}\right)^w \tag{115}$$

$$\sigma = \sigma_0 \left(\frac{m}{m_0}\right)^s \tag{116}$$

$$S = S_0 \left(\frac{m}{m_0}\right)^\alpha . \tag{117}$$

The subscript '0' denotes values for an arbitrarily chosen scaling mass. Since smaller bodies are more abundant than larger ones, we safely assume that most collisions involve a large mass ratio. In addition, we assume $w < 0$, since we expect energy equipartition to some degree in most cases. These restrictions lead to the following simplifications ($m_1 > m_2$):

$$\sigma(m_1, m_2) \approx \sigma(m_1) \tag{118}$$

$$v_{\rm rel} \approx v(m_2) \tag{119}$$

$$\epsilon \approx \frac{1}{2}\frac{m_2 \rho v_{\rm rel}^2}{m_1 S_1}. \tag{120}$$

Therefore, the smaller body m_2 enters only through the specific energy ϵ:

$$F_m \approx -\iint n(t, m_1) n(t, m_2) \sigma(m_1) v_{\rm rel}(m_2) m_1 \times f_m(m_1/m, \epsilon) {\rm d}m_1 {\rm d}m_2. \tag{121}$$

We introduce new dimensionless quantities with the help of equations (118)–(120) to simplify the integral:

$$m_1 = m x_1$$

$$m_2 = m_0 \left(\frac{m_1}{m_0}\right)^{\frac{1+\alpha}{1+2w}} \left(\frac{2S_0}{\rho v_0^2}\right)^{\frac{1}{1+2w}} \epsilon^{\frac{1}{1+2w}}. \tag{122}$$

Again, we assume a power law for the density $n \propto m^{-k}$ and change the integration parameters to (x_1, ϵ). Applying the constant-flux condition yields the equilibrium exponent

$$k \approx \frac{s + 3 + \alpha + w(2s + \alpha + 5)}{2 + \alpha + 2w} \tag{123}$$

and the scaling exponent k' of the total mass-loss

$$k' \approx \frac{s - w + 1}{2 + \alpha + 2w}$$

$$\frac{\partial}{\partial t} M_{\rm tot} \propto -\tilde{S}^{-k'} \qquad \tilde{S} = \frac{2S_0}{\rho v_0^2}. \tag{124}$$

The exponent k' in equation (124) is close to unity for realistic values of the free parameters. Thus, the mass-loss is roughly inversely proportional to the strength of the bodies. The general formula equation (123) contains the special solution of O'Brien (2003), who concentrated on the parameters $s = 2/3$, $w = 0$ and a special collisional model. In fact, the derivation applies to a much wider class of collisional models that we denote as scalable collisional models. Scalable indicates that the model is self-similar except a scaling of the impactor mass.

7 PERTURBATION OF EQUILIBRIUM

The derived scaling relations provide insight into the overall properties of a collisional cascade, which is in (or close to) equilibrium. However, they do not provide information on how the equilibrium is attained or how the system responds to various external perturbations. A rigorous approach would be the approximate solution of the coagulation equation[11], which is by no means simple since it requires a careful analysis of the collision model.

Hence, we turn to perturbations of the equilibrium size distribution, as it is easier to assess the quality of the derived expression for a variety of collision models. In addition, all equations are linear in the perturbation, allowing the detailed analysis of the solution.

If the equilibrium solution $n(m) = n_0(m/m_0)^{-k}$ is perturbed with a small deviation $\Delta n(m)$, we get to first order:

$$0 = \frac{\partial}{\partial t} m \Delta n(m) + \frac{\partial}{\partial m} F_{\rm p}(t, m)$$

$$F_{\rm p} = -\iint \Delta n(m_1) n(t, m_2) \sigma(m_1, m_2) v_{\rm rel} \times (M_{\rm red}(m, m_1, m_2) + M_{\rm red}(m, m_2, m_1)) {\rm d}m_1 {\rm d}m_2. \tag{125}$$

Despite of the expansion in Δn, equation (125) is still a complicated integro-differential equation. Thus, it is not possible to obtain a solution without further information about the problem. While there is no general solution, we restrict our attention to self-similar collisional processes. In virtue of this assumption, it is possible to simplify equation (125), as we can see in equations (126) and (126). In those expressions

$$0 = \frac{\partial}{\partial t} m \Delta n(m) - n_0 m_0^3 \sigma_0 v_0 \frac{\partial}{\partial m} \times \int \Delta n(t, m x_1) F(x_1) (m x_1/m_0)^k {\rm d}x_1 \tag{126}$$

$$F(x_1) = \int m_0^{2k-3} x_1^{-k} x_2^{-k} \frac{\sigma(x_1, x_2)}{\sigma_0} \frac{v_{\rm rel}}{v_0} \times (f_m(x_1, x_2) + f_m(x_2, x_1)) {\rm d}x_2, \tag{127}$$

where σ_0 and v_0 are velocity and cross-section of an arbitrarily chosen scaling mass m_0. $F(x_1)$ contains all information about the collisional process. If collisions do not result in extreme outcomes, like cratering or a complete destruction of the target, most of the fragment mass is contained in bodies with similar size as the parent body. Hence, we expect that $F(x_1)$ peaks around $x_1 \approx 1$ and drops to zero as x_1 gets larger (or smaller). We introduce the dimensionless relative perturbation $g(m)$:

$$g(m) = \frac{\Delta n(m)}{n(m)} = \frac{\Delta n(m) m^k}{n_0 m_0^k}. \tag{128}$$

[11] Appendix C highlights a possible approach.

Downloaded from http://mnras.oxfordjournals.org/ at MPI Gravitational Physics on January 13, 2015

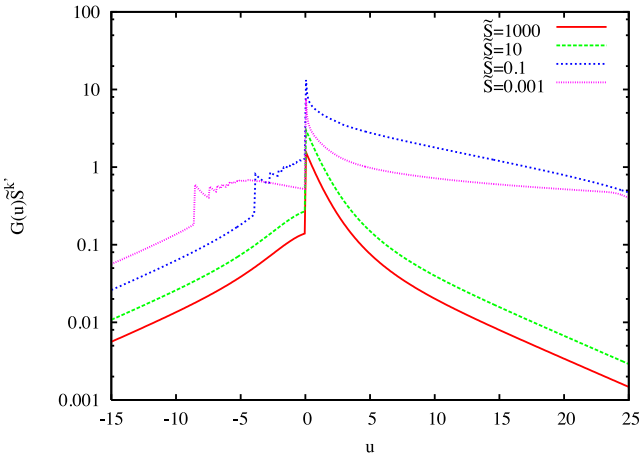

Figure 8. Scaled fragmentation kernel $G(u)$ for a simple fragmentation model (see equation 160) and different scaled impact strength $\tilde{S}$.

Thus, the new differential equation reads:

$$0 = \frac{\partial}{\partial t}(m/m_0)^{1-k}\Delta g(m) - n_0 m_0^2 \sigma_0 v_0 \frac{\partial}{\partial m}\int \Delta g(t, m x_1) F(x_1)\,\mathrm{d}x_1. \tag{129}$$

We change to logarithmic coordinates to arrive at a convolution integral:

$$u = \ln(m/m_0) \qquad u_1 = \ln(x_1). \tag{130}$$

Furthermore, we define a collisional time-scale τ_0

$$\tau_0 = (n_0 m_0 \sigma_0 v_0)^{-1} \tag{131}$$

to obtain a more concise expression. The transformed equation is

$$0 = \frac{\partial}{\partial t} g(t, u)\mathrm{e}^{u(2-k)} - \frac{1}{\tau_0}\frac{\partial}{\partial u}\int g(t, u + u_1) G(u_1)\mathrm{d}u_1 \tag{132}$$

$$G(u) = F(\mathrm{e}^u)\mathrm{e}^u. \tag{133}$$

If $g(u)$ is varying on a scale larger than the width of the kernel $G(u)$ (compare Fig. 8), it is justified to expand $g(u)$ under the integral. We retain the first two moments of $G(u)$:

$$0 = \frac{\partial}{\partial t} g(t, u)\mathrm{e}^{u(2-k)} - \frac{G_0}{\tau_0}\frac{\partial}{\partial u} g(t, u) - \frac{G_1}{\tau_0}\frac{\partial^2}{\partial u^2} g(t, u) \tag{134}$$

$$G_k = \int u^k G(u)\,\mathrm{d}u. \tag{135}$$

The first-order moment G_1, which introduces a diffusive term, is omitted in the following for clarity[12]. We introduce a fragmentation time $\tau_{\mathrm{frag}}(u)$ and transform equation (134) back to m:

$$0 = \frac{\partial}{\partial t} g(t, m) - \frac{m}{\tau_{\mathrm{frag}}(m)}\frac{\partial}{\partial m} g(t, m) \tag{136}$$

$$\tau_{\mathrm{frag}} = \frac{\tau_0}{G_0}\mathrm{e}^{u(2-k)} = \frac{\tau_0}{G_0}(m/m_0)^{2-k}. \tag{137}$$

Equation (136) is a modified advection equation, which conserves the total mass. It is possible to derive equations similar to equation (136) for any collisional model. However, the general approach is less fruitful, as it lacks a robust frame of a known equilibrium solution and reliable scaling relations. Therefore, we provide only the extension to scalable collisional models in Appendix B. We readily obtain the general solution

$$g(t, m) = f\left(t + \tau_0 \frac{(m/m_0)^{(2-k)}}{G_0(2-k)}\right)$$

$$\Delta n(t, m) = n(m) f\left(t + \tau_0 \frac{(m/m_0)^{(2-k)}}{G_0(2-k)}\right). \tag{138}$$

The function f is determined by the initial value $g(0, m)$ of the perturbation. As the collisional cascade evolves, the initial perturbation function is shifted as a whole to smaller masses. This evolution becomes clearer if we attach labels $M(0)$ to the initial perturbation function and follow the time evolution of these tags. The functions $M(t)$ are the characteristics[13] of the differential equation (136):

$$M(t) = m_0\left[(M(0)/m_0)^{(2-k)} - t/\tau_0 G_0(2-k)\right]^{1/(2-k)}. \tag{139}$$

The meaning of the fragmentation time τ_{frag} becomes clear by the relation

$$\frac{M}{\dot{M}} = -\tau_{\mathrm{frag}} \tag{140}$$

which is the time until a body has lost a significant fraction of its mass due to destructive collisions. A comparison of the perturbation equation (136) with the scaling relations from the previous section gives the scaling of the zeroth-order moment G_0 with respect to the impact strength:

$$G_0 = G_0' \tilde{S}^{-k'}. \tag{141}$$

G_0' should only depend on the fragmentation model (i.e. fragment size distribution as a function of the largest fragment f_1) within the limits of this approximation. Fig. 8 shows that the scaling with the impact strength works quite well, except slight variations which are small compared to the covered range of impact strengths. Likewise, it is possible to restate the total equilibrium flux F_{eq} in terms of G_0':

$$F_{\mathrm{eq}}(m) \approx -\frac{G_0'}{2} n(m)^2 \sigma(m) m^3 v_{\mathrm{rel}} \tilde{S}^{-k'}. \tag{142}$$

The fragmentation time-scale $\tau_{\mathrm{frag}}(m)$ allows a more intuitive expression:

$$F_{\mathrm{eq}}(m) \approx -\frac{1}{2}\frac{n(m)m^2}{\tau_{\mathrm{frag}}(m)}. \tag{143}$$

Our simple collisional model (see Fig. 8 and equation 160) refers to

$$F_{\mathrm{eq}}(m) = -(1\ldots 30) \times n(m)^2 \sigma(m) m^3 v_{\mathrm{rel}} \tilde{S}^{-k'}. \tag{144}$$

8 MIGRATION AND COLLISIONS

The local perturbation analysis is only applicable to a planetesimal disc if the migration velocity of the planetesimals is negligibly small. This assures that collisional cascades at different radial distances do not couple to each other, so that the whole disc is composed of many local cascades. While this assumption is justified for larger

[12] The study of wave-like structures in the size distribution (see e.g. Bagatin et al. 1994) requires even the second-order moment G_2.

[13] In general, characteristics of a partial differential equation are paths along which the solution is constant.

Downloaded from http://mnras.oxfordjournals.org/ at MPI Gravitational Physics on January 13, 2015

bodies, migration strongly influences bodies below 1 km in size. Hence, we must extend our analysis to examine the influence of migration on the (no longer) local collisional processes.

We assume that the collisional evolution of the system leads to an equilibrium planetesimal distribution everywhere in the disc:

$$\Sigma_0(r, m) = \Sigma_{r,0}(r) C_0(m), \tag{145}$$

where $\Sigma_r(r)$ is the total surface density at a given distance r, while $C_0(m)$ is the universal equilibrium distribution. Though the planetesimal distribution at larger sizes is likely different at different locations in the disc, we only demand a universal function at smaller sizes, where migration is important. The power-law exponent k depends on the details of the invoked physics, but numerical simulations show that $k \approx 2$ is a fiducial value. Equation (145) does not yet include migration effects. If we include migration, the surface density is modified to

$$\Sigma(r, m) = g(r, m)\Sigma_0(r, m), \tag{146}$$

where the dimensionless function g contains the changes due to migration. The collisional evolution is governed by the continuity equation with an additional collisional term

$$\frac{\partial \Sigma(r, m)}{\partial t} - \frac{1}{r}\frac{\partial}{\partial r}\left(v(r, m) r \Sigma(r, m)\right) = \dot{\Sigma}_{\rm coll}, \tag{147}$$

where $v(r, m)$ is the migration velocity (see equation 41), defined such that positive v imply an inward migration. We express the collisional term with the help of equation (136) and seek for a steady-state solution $\dot{\Sigma} = 0$:

$$\frac{1}{\tau_{\rm frag}(m, r)}\frac{\partial g}{\partial m} m \Sigma_{r,0}(r) + \frac{1}{r}\frac{\partial}{\partial r}\left(g v r \Sigma_{r,0}(r)\right) = 0, \tag{148}$$

where $\tau_{\rm frag}(m, r)$ is the fragmentation time-scale of a mass m at a distance r. Since the surface density Σ and the various contributions to the drag force are well described by a power law (with respect to radius), equation (148) further simplifies to

$$\frac{1}{\tau_{\rm frag}(m, r)}\frac{\partial g}{\partial m} m + \frac{\partial g}{\partial r} v - \frac{b}{r} g v = 0, \tag{149}$$

where b is a combination of the various invoked power-law exponents. As the surface density Σ and the gas density drop with increasing radius in any realistic disc model, it is safe to assume $b > 0$. We choose a self-similar ansatz for g:

$$g(r, m) = g(\zeta) \quad , \quad \zeta = m g_m(r). \tag{150}$$

The new differential equation is

$$\frac{1}{\tau_{\rm frag}(m, r)}\frac{{\rm d}g}{{\rm d}\zeta} m g_m(r) + m \frac{{\rm d}g}{{\rm d}\zeta}\frac{{\rm d}g_m}{{\rm d}r} v - \frac{b}{r} g v = 0 \tag{151}$$

which is equivalent to the more concise expression:

$$\frac{{\rm d}\ln(g)}{{\rm d}\ln(\zeta)}\left(\frac{r}{v\tau_{\rm frag}} + \frac{{\rm d}\ln(g_m)}{{\rm d}\ln(r)}\right) = b. \tag{152}$$

We assume a power-law dependence for the time-scale ratio $\tau_{\rm mig}/\tau_{\rm frag}$:

$$\frac{r}{v\tau_{\rm frag}} = \frac{\tau_{\rm mig}}{\tau_{\rm frag}} = (m/m_0)^{k_m}(r/r_0)^{k_r}. \tag{153}$$

The cut-off mass m_0 at a distance r_0 has a time-scale ratio $\tau_{\rm mig}/\tau_{\rm frag} = 1$, which defines a proper lower cut-off within this context. Hence, the solution is

$$b = \frac{{\rm d}\ln(g)}{{\rm d}\ln(\zeta)}\left(\zeta^{k_m} + \frac{k_r}{k_m}\right) \tag{154}$$

$$g_m(r) = \frac{(r/r_0)^{k_r/k_m}}{m_0} \tag{155}$$

$$g(\zeta) = \left(1 + \frac{k_r}{k_m \zeta^{k_m}}\right)^{-b/k_r}. \tag{156}$$

Though the analytical solution equation (156) provides a complete description of the lower cut-off of the size distribution, it is more appropriate within the frame of this discussion to translate the equilibrium solution to an equilibrium mass-loss due to migration:

$$\begin{aligned}\dot{\Sigma}_{\rm mig}(r, m) &= -\frac{bv}{r}\Sigma + \frac{bv}{r}\Sigma\frac{k_r/k_m}{\zeta^{k_m} + k_r/k_m} \\ &= -\frac{b\Sigma}{\tau_{\rm mig} + k_r/k_m \tau_{\rm frag}}.\end{aligned} \tag{157}$$

An inspection of the time-scale ratio shows that the mass exponent k_m should be positive, whereas simple estimations of k_r on the basis of the minimum-mass solar nebula are somewhat inconclusive. The value of k_r is so close to zero that any change in the assumed equilibrium slope or the impact strength scaling gives easily both positive and negative values. Moreover, equation (157) requires a globally relaxed planetesimal disc, but the huge spread in the various involved time-scales at different radii inhibits any significant relaxation in the early stages.

However, it is possible to gain valuable information from the two limiting cases $k_r > 0$ and $k_r < 0$. Both values of k_r give the proper limit $g \to 1$ at large masses, where the migration time-scale is much larger than the fragmentation time-scale and we recover the steady-state collisional cascade.

A positive exponent k_r reduces the effective mass-loss due to migration, as fragments from the outer part of the disc replenish the local mass-loss. Hence, the fragmentation time-scale controls the net loss of smaller planetesimals. In contrast, a negative exponent k_r leads to a pronounced cut-off in the size distribution, since only larger planetesimals are replenished through inward migration. Though the mass-loss rate is singular at some mass m', this sharp cut-off is an artefact due to the perturbation approximation.

Our analysis is subjected to several restrictions. We applied the perturbation equation to values of g that exceed the limit for a safe application (i.e. $g \not\approx 1$) of the perturbation expansion. Furthermore, the steady-state solution requires a global relaxation of the collisional processes, which is practically never obtained during the disc evolution. Despite of these restrictions, we gained insight on a more qualitative level. Numerical calculations indicate that the perturbation approximation is inappropriate close to the lower cut-off of the size distribution. However, a comparison of different exponents k_r (see Fig. 9) attributes only a minor role to the replenishment of fragments due to inward migration. Only unrealistic small slopes b of the migrational mass influx would strengthen the importance of this process. Though temporally non-equilibrium phenomena are not ruled out by the previous derivation, their study would require the global simulation of the system.

9 CHOICE FOR THE COLLISIONAL MODEL

Any detailed study of a collisional system requires the specification of a realistic collisional model. We first subtract the well-known perfect accretion model. While it is an oversimplification for collisions among kilometre-sized planetesimals, its simplicity

Downloaded from http://mnras.oxfordjournals.org/ at MPI Gravitational Physics on January 13, 2015

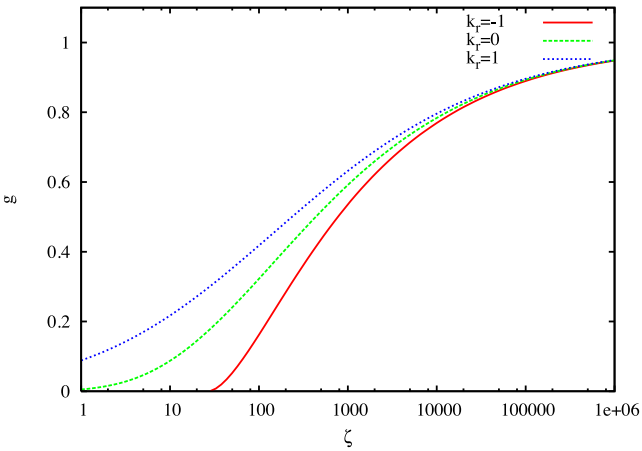

Figure 9. Cut-off function g according to equation (156). The mass exponent is $k_m = 1/3$, while the mass influx exponent is $b = 1.75$ according to the minimum solar nebula.

allows a reliable code testing and eases the comparison with other works:

$$M_{\rm red}(m, m_1, m_2) = -m_1\Theta(m - m_1) - m_2\Theta(m - m_2) + (m_1 + m_2)\Theta(m - m_1 - m_2). \quad (158)$$

Although our fragmentation model (see Section 4) provides a very detailed description of the outcome of a collision, we abandon most of the details for the following reasons. The computational effort of the numerical solution of the coagulation equation scales with the third power of the number of mass bins. Hence, we choose a mass grid whose resolution is by far smaller than the information provided by the detailed collisional model. As a mismatch of the mass resolution could produce undesired artefacts, a lower resolution of the collisional model is needed for consistence. Thus, only the largest fragment $f_1(f_1^i, \gamma)$ and the second fragment $f_1^{(2)}(f_1^i, \gamma)$ (which contains information on reaccumulation) enter the fragment size distribution:

$$\frac{M_{\rm red}(xM)}{M} = \begin{cases} 1 & \text{if } x \geq f_1 \\ 1 - f_1 & \text{if } f_1 > x \geq f_1^{(2)} \\ (1 - f_1 - f_1^{(2)})(x/f_1^{(2)})^{f_1} & \text{otherwise} \end{cases}. \quad (159)$$

Both values f_1 and $f_1^{(2)}$ are interpolated from Table 7, where the initial fragment size $f_1^{\rm i}$ is calculated from the dimensionless impact energy ϵ. We used a reduced fragmentation model for test purposes:

$$M_{\rm red}(xM)/M = \begin{cases} 1 & \text{if } x \geq f_1 \\ (1 - f_1)(x/f_1)^{f_1} & \text{otherwise} \end{cases}. \quad (160)$$

Table 8 summarizes the most important model parameters.

Table 8. Main parameters of the collisional model.

ρ	2700 kg m^{-3}
k	1/6
Model	Gaussian scatter
$f_{\rm KE}$	0.1
K	1.24

We note that $M_{\rm red}$ is defined in such a way that the equations conserve the mass (see equation 100). Also, by using f_1 and $f_1^{(2)}$, we avoid the problem that is inherent to using only f_1: namely that the exponent of the distribution of fragmentation is $1 - f_1$, which goes to 0 in the cratering limit.

10 STATISTICAL MODEL

We work out a scheme to integrate the evolution of particle number and velocities in our coagulation code. Our implementation follows the standard procedure of former works, such as Hornung, Pellat & Barge (1985). The direct approach to the integration of an N-body system is, in principle, possible for any particle number. This procedure becomes computationally too expensive for very large particle numbers. In the following of this section, we employ the usual notation as followed by e.g. Binney & Tremaine (2008), in their description of the Fokker–Planck equation, and will avoid usual equations that can be found in that one or any other text book.

Instead of tracking all particle orbits, we can define a distribution function f (a phase-space density), which gives the probability to find a particle at a position $\boldsymbol{x}$ with a velocity $\boldsymbol{v}$, i.e. the state of the system. As long as only dynamical interactions are taken into account, the number of all particles (e. g. stars, planetesimals) is conserved. f is a function of six variables, so an exact solution is usually very complicated or even impossible. However, it is possible to gain valuable insight into the problem by taking the moments of the distribution function (see Schneider, Amaro-Seoane & Spurzem 2011):

$$\langle x_i^n v_j^m \rangle = \int f(\boldsymbol{x}, \boldsymbol{v}) x_i^n v_j^m \mathrm{d}^3x \mathrm{d}^3v \qquad n, m > 0. \quad (161)$$

The first-order moment with respect to velocity gives the time evolution of the mean velocity $\bar{v}$:

$$\nu \frac{\partial \bar{v}_j}{\partial t} + \nu \bar{v}_i \frac{\partial \bar{v}_j}{\partial x_i} = -\nu \frac{\partial \Phi}{\partial x_j} - \frac{\partial(\nu \sigma_{ij}^2)}{\partial x_i} + \nu \left(\frac{\partial \bar{v}_j}{\partial t}\right)_{\rm coll} \quad (162)$$

$$\bar{v}_i = \frac{1}{\nu} \int f(\boldsymbol{x}, \boldsymbol{v}) v_i \mathrm{d}^3v$$

$$\sigma_{ij}^2 = \overline{v_i v_j} - \bar{v}_i \bar{v}_j, \quad (163)$$

where σ_{ij} is the anisotropic velocity dispersion and the continuity equation was used to arrive at a more concise formulation. While the structure of the moment equations is already familiar from hydrodynamics, they do not provide a closed set of differential equations, since each differential equation of a given moment is related to (yet unknown) higher order moments. Hence, any finite set of momenta needs a closure relation – additional constraints that relate the highest order moments to known quantities. The choice of this relation is a key element in the validity of the equations, but it is not unique and depends well on the problem at hand (compare e.g. Larson 1970).

10.1 Distribution function

Any statistical description of a planetesimal disc requires the knowledge of the distribution function. Since the full problem including collisions, encounters and gas drag has no analytic solution, a collisionless planetesimal disc (i.e. no perturbations) is a natural basis for further investigations. The distribution function that describes such a simplified system is a solution of the Boltzmann equation.

Downloaded from http://mnras.oxfordjournals.org/ at MPI Gravitational Physics on January 13, 2015

A special solution to the Boltzmann equation is a thin homogenous planetesimal disc

$$f(z, v) = \frac{\Omega\Sigma}{2\pi^2 T_\mathrm{r} T_z m} \exp\left(-\frac{v_\mathrm{r}^2 + 4v_\phi^2}{2T_\mathrm{r}} - \frac{v_z^2 + \Omega^2 z^2}{2T_z}\right) \tag{164}$$

provided that the radial velocity dispersion T_r and the vertical dispersion T_z are small compared the mean orbital velocity v_K. The azimuthal velocity dispersion T_ϕ is locked to T_r by the local epicyclic frequency κ in a central potential, where the ratio 1 : 4 is a special solution of (see e.g Binney & Tremaine 2008) $\kappa^2 T_\mathrm{r} = 4\Omega^2 T_\phi$. All velocities v_r, v_ϕ and v_z refer to the local Keplerian velocity. The normalization is the same as in Stewart & Ida (2000). A planetesimal disc is a slowly evolving system compared to the orbital time, hence it is reasonable to use equation (164) as a general solution of the perturbed problem. Σ, T_z and T_r are now functions of time and of the radial distance to the star. All information on the system is contained in these three momenta of the distribution function, where higher order moments can be deduced from equation (164). Thus, the functional form of the distribution function represents an implicit closure relation.

The validity of this approximation can be further assessed by a closer examination of the Boltzmann equation. We summarize all perturbations in an evolution time-scale T_evol and reduce the radial structure to some typical length-scale Δr to estimate the deviation from the functional form equation (164). A comparison with the Boltzmann equation shows that the difference is small if the migration time-scale and the evolution time-scale are large compared to the orbital time T_0, $T_0 \ll \Delta r/\langle v_\mathrm{r}\rangle$ and $T_0 \ll T_\mathrm{evol}$. An order-of-magnitude estimate of the evolution time supports these requirements. Furthermore, numerical calculations confirm that the velocity distribution stays triaxial Gaussian (see Ida 1992).

The distribution function is equivalent to an isothermal vertical density structure with scaleheight h:

$$h = \sqrt{\frac{T_z}{\Omega^2}} \tag{165}$$

$$\rho(z) = \rho_0 \exp\left(-\frac{z^2}{2h^2}\right). \tag{166}$$

Thus, the central density ρ_0 and the mean density $\langle\rho\rangle$ are related to the surface density in a simple way:

$$\rho_0 = \frac{\Sigma}{\sqrt{2\pi}h}$$
$$\langle\rho\rangle = \frac{\rho_0}{\sqrt{2}}. \tag{167}$$

The triaxial Gaussian velocity distribution is equivalent to a Rayleigh distribution of the orbital elements e and i[14]:

$$\mathrm{d}n(e^2, i^2) = \frac{1}{\langle e^2\rangle\langle i^2\rangle} \exp\left(-\frac{e^2}{\langle e^2\rangle} - \frac{i^2}{\langle i^2\rangle}\right) \mathrm{d}e^2 \mathrm{d}i^2$$
$$\langle e^2\rangle = \frac{2T_\mathrm{r}}{(\Omega r_0)^2} \qquad \langle i^2\rangle = \frac{2T_z}{(\Omega r_0)^2}. \tag{168}$$

Planetesimal encounters couple the time evolution of eccentricity and inclination, so that the ratio i^2/e^2 tends to an equilibrium value after a few relaxation times. It is close to 1/4 in a Keplerian potential, but the precise value also depends on the potential itself (Ida et al. 1993).

[14] Equations (3)–(5) provide the coordinate transformation.

10.2 Dynamical friction

The Coulomb logarithm in the standard formulation of Chandrasekhar (1942), Λ, arises from an integration over all impact parameters smaller than an upper limit l_max, given by

$$\Lambda \approx \frac{\sigma_\mathrm{v}^2 l_\mathrm{max}}{G(m+M)}. \tag{169}$$

Although encounters in the gravitational field of the sun deviate from pure two-body scatterings, it is safe to neglect the presence of the sun if the encounter velocity is large compared to the Hill velocity[15] ΩR_Hill. Thus, the classical dynamical friction formula is also applicable to planetesimal encounters in the high-velocity regime, though a generalization to triaxial velocity distributions σ_i is necessary (see e.g. Binney 1977). An additional complication is the choice of l_max (i.e. the choice of the Coulomb logarithm). There are several scalelengths, which could determine the largest impact parameter l_max: the scaleheight of the planetesimal disc, the radial excursion due to the eccentric motion of the planetesimals and the Hill radius of the planetesimals. As it is not possible to derive a unique expression for l_max from first principles, a proper formula is often fitted to N-body calculations (compare equation 173). The velocity dispersion of a planetesimal disc is triaxial with $T_\phi/T_\mathrm{r} = 1/4$ and $T_z/T_\mathrm{r} \approx 1/4$. We take these values and expand the set of equations of Binney (1977) for small velocities v_M:

$$\frac{\mathrm{d}v_{M,\mathrm{r}}}{\mathrm{d}t} \approx -1.389\, v_{M,\mathrm{r}} \frac{\sqrt{2\pi}G^2 \ln(\Lambda)(M+m)n_0\, m}{T_\mathrm{r}^{3/2}}$$
$$\frac{\mathrm{d}v_{M,\phi}}{\mathrm{d}t} \approx -3.306\, v_{M,\phi} \frac{\sqrt{2\pi}G^2 \ln(\Lambda)(M+m)n_0\, m}{T_\mathrm{r}^{3/2}}$$
$$\frac{\mathrm{d}v_{M,z}}{\mathrm{d}t} \approx -3.306\, v_{M,z} \frac{\sqrt{2\pi}G^2 \ln(\Lambda)(M+m)n_0\, m}{T_\mathrm{r}^{3/2}}. \tag{170}$$

The derived expressions provide a compact tool to analyse dynamical friction in disc systems. However, the involved approximations are too severe compared to the needs of an accurate description. While these concise expressions are valuable for basic estimations, the following sections derive viscous stirring and dynamical friction formulae for a planetesimal system in a rigorous way.

10.3 High-speed encounters

We return to the Boltzmann equation as a starting point for the derivation of the scattering coefficients. Again, we omit the basic formulae that can be found in any textbook and employ the usual notation and terminology. In virtue of the ansatz for the distribution function (see equation 164), it is sufficient to derive the time derivative of the second-order velocity moments T_r and T_z. Since the distribution function is time independent in the absence of encounters, only the collisional term contributes to the time derivative of the velocity dispersions T_k ($k \in (r, z, \phi)$ in the following:

$$\frac{\mathrm{d}\rho T_k}{\mathrm{d}t} = \int \mathrm{d}^3 v m v_k^2 \left(\frac{\partial f}{\partial t}\right)_\mathrm{coll}. \tag{171}$$

The collisional term invokes the averaging over many different scattering trajectories and is, given that the underlying encounter model is analytically solvable, still too complex to derive an exact expression. If most of the encounters are weak – a realistic

[15] Whenever relative velocities are classified as 'high' or 'low' in the following sections, a comparison with the Hill velocity is implied.

Downloaded from http://mnras.oxfordjournals.org/ at MPI Gravitational Physics on January 13, 2015

assumption in a planetesimal disc – it is possible to expand the collisional contribution in terms of the velocity change Δv_i. This is the usual Fokker–Planck approximation (see e.g. Binney & Tremaine 2008). The diffusion coefficients D contain all information on the underlying scattering process. The usual next step is to consider two interacting planetesimal populations m, m^* with distribution functions

$$f = \frac{\Omega\Sigma}{2\pi^2 T_\mathrm{r} T_z m} \exp\left(-\frac{v_\mathrm{r}^2 + 4v_\phi^2}{2T_\mathrm{r}} - \frac{v_z^2 + \Omega^2 z^2}{2T_z}\right)$$

$$f^* = \frac{\Omega\Sigma^*}{2\pi^2 T_\mathrm{r}^* T_z^* m^*} \exp\left(-\frac{v_\mathrm{r}^2 + 4v_\phi^2}{2T_\mathrm{r}^*} - \frac{v_z^2 + \Omega^2 z^2}{2T_z^*}\right) \tag{172}$$

to be able to evaluate the terms in the Fokker–Planck approximation. In this regard, we follow in our approach the scheme of Stewart & Ida (2000) except some minor changes in the notation, and refer the reader to their work for more details.

The determination of a proper Coulomb logarithm Λ leaves room for further optimization. A careful comparison with N-body models gives rise to the empirical choice (Ohtsuki, Stewart & Ida 2002):

$$\Lambda = \frac{1}{12}(\langle\tilde{e}^2\rangle + \langle\tilde{i}^2\rangle)\langle\tilde{i}^2\rangle^{1/2} \tag{173}$$

$$\tilde{e} = \frac{\sqrt{2T_\mathrm{r}}}{\Omega R_\mathrm{Hill}} \qquad \tilde{i} = \frac{\sqrt{2T_z}}{\Omega R_\mathrm{Hill}}. \tag{174}$$

Ohtsuki et al. (2002) also report a further improvement by setting $B \equiv A$.

10.4 Low-speed encounters

Encounters in the low-velocity regime exhibit a wealth of different orbits, as the solar gravity field perturbs the two-body scattering. Only a small subset of the trajectories represents simple, regular orbits like Tadpole or Horseshoe orbits[16]. Hence, an examination of this velocity regime is best done by integrating the equations of motions numerically.

Ohtsuki et al. (2002) integrated a large set of planetesimal encounters and extracted fitting formulae that cover the low-velocity regime. Their expressions for viscous stirring are given in their work. The stirring rate of the radial velocity dispersion approaches a finite value for very low velocity dispersions, while the stirring rate for the vertical velocity dispersion drops to zero as the velocity dispersion decreases. This different behaviour of the two limits is due to the encounter geometry: if two planetesimals have zero inclination, they may still excite higher eccentricities during an encounter, but they remain confined to the initial orbital plane preventing any excitation of inclinations.

As the stirring rates are only valid in the low-velocity regime, Ohtsuki et al. (2002) introduced special interpolation coefficients C_i. These coefficients tend to unity for very small velocity dispersions, and drop to zero in the high-velocity regime. Thus, the interpolation formulae are properly 'switched off' in the high-velocity regime, so they do not interfere with the known high-velocity stirring rates.

10.5 Distant encounters

All formulae include only the stirring rates due to close encounters, but non-crossing orbits also contribute to the overall change of the velocity distribution. As these distant encounters lead to small changes of the orbital elements, the problem is accessible to perturbation theory; see Hasegawa (1990) for a detailed treatment. Stewart & Ida (2000) integrated the perturbation solution over all impact parameters to derive the collective effect of all distant encounters:

$$\frac{\mathrm{d}\langle e^2\rangle}{\mathrm{d}t} = \frac{\Omega m^* \Sigma^* r_0^2}{(m+m^*)^2}\langle P_\mathrm{VS,dist}\rangle$$

$$\langle P_\mathrm{VS,dist}\rangle = 7.6\frac{\alpha(m+m^*)^2}{M_\mathrm{c}^2} \times \frac{\mathrm{EXINT}\left(\alpha\frac{h^2}{(\langle e^2\rangle+\langle e^{*2}\rangle)}\right) - \mathrm{EXINT}\left(\alpha\frac{h^2}{(\langle i^2\rangle+\langle i^{*2}\rangle)}\right)}{\langle e^2\rangle + \langle e^{*2}\rangle - \langle i^2\rangle - \langle i^{*2}\rangle}$$

$$\mathrm{EXINT}(x) := \exp(x)\Gamma(0,x) \qquad h = \sqrt[3]{\frac{m+m^*}{3M_\mathrm{c}}}$$

$$\alpha \approx 1, \tag{175}$$

where α accounts for the uncertainty in the smallest impact parameter that is regarded as a distant encounter. While distant encounters are already included in the interpolation formula of the low-velocity regime, we use the modified expression:

$$\left(\frac{\mathrm{d}T_\mathrm{r}}{\mathrm{d}t}\right)_\mathrm{dist} = \frac{1}{2}(\Omega r_0)^2\left(\frac{\mathrm{d}\langle e^2\rangle}{\mathrm{d}t}\right)_\mathrm{dist}(1-C_1) = \frac{GM_\mathrm{c} r_0 \Omega m^* \Sigma^*}{2(m+m^*)^2}\langle P_\mathrm{VS,dist}\rangle(1-C_1). \tag{176}$$

Stewart & Ida (2000) omitted the change in the inclination, as it is small due to the encounter geometry. We derive here the integrated stirring rate for completeness, in the lengthy equation (177).

$$\frac{\mathrm{d}\langle i^2\rangle}{\mathrm{d}t} = \frac{\Omega m^* \Sigma^* r_0^2}{(m+m^*)^2}\langle Q_\mathrm{VS,dist}\rangle\langle Q_\mathrm{VS,dist}\rangle = 0.4\frac{\alpha^2(m+m^*)^2}{M_\mathrm{c}^2} \times \frac{1}{\langle e^2\rangle + \langle e^{*2}\rangle - \langle i^2\rangle - \langle i^{*2}\rangle} \times \left[1 - \frac{\alpha h^2}{\langle i^2\rangle + \langle i^{*2}\rangle}\mathrm{EXINT}\left(\alpha\frac{h^2}{(\langle i^2\rangle + \langle i^{*2}\rangle)}\right) - (\langle i^2\rangle + \langle i^{*2}\rangle)\frac{\mathrm{EXINT}\left(\alpha\frac{h^2}{(\langle e^2\rangle+\langle e^{*2}\rangle)}\right) - \mathrm{EXINT}\left(\alpha\frac{h^2}{(\langle i^2\rangle+\langle i^{*2}\rangle)}\right)}{\langle e^2\rangle + \langle e^{*2}\rangle - \langle i^2\rangle - \langle i^{*2}\rangle}\right]. \tag{177}$$

A close inspection of the integrated perturbation shows that the above formula is roughly a factor $\langle i^2\rangle + \langle i^{*2}\rangle$ smaller than the corresponding changes in the eccentricity.

10.6 Gas damping

The presence of a gaseous disc damps the velocity dispersion of the planetesimals and introduces a slow inward migration. Adachi et al. (1976) used the drag law equation (39) to approximate[17] the

[16] The most famous example of such a regular orbit are the two Saturnian moons Janus and Epimetheus which share nearly the same orbit.

[17] A formal expansion at $e = 0$, $i = 0$, $\eta_\mathrm{g} = 0$ is not possible, since the drag law involves the modulus of the relative velocity. Kary, Lissauer & Greenzweig (1993) corrected a missing factor 3/2 in equation (178).

Downloaded from http://mnras.oxfordjournals.org/ at MPI Gravitational Physics on January 13, 2015

average change of the orbital elements:

$$\tau_0 = \frac{2m}{\pi C_D \rho_g R^2 v_K} \qquad \eta_g = \frac{|v_K - v_g|}{v_K}$$

$$\frac{d}{dt} e^2 \approx -\frac{2e^2}{\tau_0}\left(0.77\,e + 0.64\,i + \frac{3}{2}\eta_g\right) \tag{178}$$

$$\frac{d}{dt} i^2 \approx -\frac{2i^2}{\tau_0}\left(0.39\,e + 0.43\,i + \frac{1}{2}\eta_g\right)$$

$$\frac{d}{dt} a \approx -\frac{2a}{\tau_0}\eta_g\left(0.97\,e + 0.64\,i + \eta_g\right) \tag{179}$$

η_g is the dimensionless velocity lag of the sub-Keplerian rotating gaseous disc.

10.7 Unified expressions

All expressions for the different velocity regimes are constructed such that a smooth transition between the different regimes is assured. Thus, a simple addition of all contributions yields already the unified expressions

$$\frac{dT_r}{dt} = \left(\frac{dT_r}{dt}\right)_{high} + \left(\frac{dT_r}{dt}\right)_{low} + \left(\frac{dT_r}{dt}\right)_{gas} + \left(\frac{dT_r}{dt}\right)_{dist} \tag{180}$$

$$\frac{dT_z}{dt} = \left(\frac{dT_z}{dt}\right)_{high} + \left(\frac{dT_z}{dt}\right)_{low} + \left(\frac{dT_z}{dt}\right)_{gas} + \left(\frac{dT_z}{dt}\right)_{dist} \tag{181}$$

which cover the full range of relative velocities. Although only two populations m and $m^\star$ were assumed, equations (180) and (181) are readily generalized to a multimass system by adding a summation over all masses.

10.8 Inhomogeneous disc

The preceding derivations assumed a homogeneous disc, which simplified the calculation, since the integration over all impact parameters needed no special precaution. A more sophisticated consequence is that the spatial density and the density in semimajor axis space are equal:

$$\Sigma(r) = \Sigma(a) = \Sigma_0. \tag{182}$$

Density inhomogeneities break this simple relation, as particles at the same radial distance could have different semimajor axes, and particles with the same semimajor axis are located at different positions at a given time. While both representations are equivalent (i.e. describe the same system in different ways), we choose the density in semimajor axis space as the primary density[18]. The spatial density is derived as

$$\Sigma(r) = \int \frac{1}{\sqrt{2\pi a^2 \langle e^2(a)\rangle}} \exp\left(-\frac{(a-r)^2}{2a^2\langle e^2(a)\rangle}\right)\Sigma(a)\,da. \tag{183}$$

Likewise, T_r and T_z are also functions of the semimajor axis.

Furthermore, an inhomogeneous surface density invalidates the averaging over all impact parameters. Planetesimal encounter are most efficient for impact parameters smaller than a few Hill radii, so the derivation is still valid if the surface density is roughly constant on that length-scale. However, a planetesimal that is large enough will 'feel' the spatial inhomogeneities or even generate density fluctuations. Hence, it is essential to extend the validity of the averaged expressions to inhomogeneous systems. We use the averaged expressions

$$\left\langle \frac{dT_{r,z}}{dt} \right\rangle = \Sigma(a)\int_{-\infty}^{\infty} \frac{d\tilde{T}_{r,z}(b)}{dt} db \tag{184}$$

as a starting point ($d\tilde{T}_{r,z}/dt$ excludes the surface density, as opposed to the averaged expressions). The (yet unknown) scattering contribution $d\tilde{T}_{r,z}/dt$ as a function of the impact parameter b is our starting point for a general expression for a varying surface density:

$$\frac{dT(a_0)_{r,z}}{dt} = \int_{-\infty}^{\infty} \Sigma(a_0 + b)\frac{d\tilde{T}_{r,z}(b)}{dt} db. \tag{185}$$

We restate equation (185) in terms of a weight function $w(b)$:

$$\frac{dT(a_0)_{r,z}}{dt} = \left\langle \frac{dT_{r,z}}{dt} \right\rangle \frac{1}{\Sigma(a_0)} \int_{-\infty}^{\infty} \Sigma(a_0 + b) w(b)\, db \tag{186}$$

$$w(b) = \Sigma(a_0)\frac{d\tilde{T}_{r,z}(b)}{dt}\left\langle \frac{dT_{r,z}}{dt} \right\rangle^{-1}. \tag{187}$$

The numerical solution of the Hill problem gives some insight into how the weight function $w(b)$ changes with the impact parameter. We follow a similar approach as in Petit (1986) for the evolution of particle densities in the Hill problem.

10.9 Diffusion coefficient

We concentrated on the evolution of the velocity dispersion so far, but scatterings among planetesimals also change the semimajor axis of the disc particles, inducing a diffusive evolution of the surface density:

$$\frac{\partial \Sigma}{\partial t} = \Delta_a(D\Sigma). \tag{188}$$

The diffusion coefficient D is related to the typical change in semimajor axis Δa and the time-scale T_{2Body} on which planetesimal encounters operate:

$$D \approx \frac{(\Delta a)^2}{T_{2Body}}. \tag{189}$$

If we neglect the radial displacement during an encounter, the change in semimajor axis is solely due to the change of the velocity:

$$-\frac{GM}{2a} = -\frac{GM}{r} + \frac{1}{2}v^2$$

$$\Delta a \approx \frac{2a^2}{GM}\boldsymbol{v}\cdot\Delta\boldsymbol{v}. \tag{190}$$

An average over all orientations of the velocity $\boldsymbol{v}$ and the velocity change $\Delta\boldsymbol{v}$ yields the mean square change in semimajor axis:

$$\langle(\Delta a)^2\rangle \approx \frac{4a^3}{3GM}\langle(\Delta v)^2\rangle$$

$$= \frac{4}{3\Omega^2}(\Delta T_r + \Delta T_\phi + \Delta T_z). \tag{191}$$

This yields the mean diffusion coefficient

$$D \approx \frac{4}{3\Omega^2}\left(\frac{5}{4}\frac{d}{dt}T_r + \frac{d}{dt}T_z\right), \tag{192}$$

[18] We denote $\Sigma(a)$ also as 'surface density' and refer to a as a radial coordinate. However, all formulae are precise in discriminating both representations in r and a.

Downloaded from http://mnras.oxfordjournals.org/ at MPI Gravitational Physics on January 13, 2015

where the time derivatives of the velocity dispersions T_r and T_z are taken with respect to encounters. We note that this approach does not replace large angle scattering by close approaches of planetesimals to large planets. However, $\dot{T}_r$ and $\dot{T}_z$ do contain large angle scattering. We note that it is important to maintain an integral number of particles as they migrate radially inward.

10.10 Coagulation equation

We treat collisions with the particle in a box method, where the collision rate is a number density times a cross-section times a relative velocity. In our scheme, we use numerical calculations from Greenberg (1991) and Greenzweig (1992)[19] as a basis for a unified fitting formula

$$\tilde{\sigma} = \sigma \times 0.572\,(1 + 3.67 v_{\rm Hill}/v_{\rm rel}) \left(1 + 1.0 \frac{\sigma \Omega^2}{T_z}\right)^{-1/2} \tag{193}$$

$$\sigma = \sigma_{\rm geom} \left(1 + \frac{v_\infty^2}{v_{\rm rel}^2 + 1.8 v_{\rm Hill}^2}\right) \tag{194}$$

$$v_{\rm rel}^2 = \frac{1}{2}(T_r + T_\phi + T_z) \qquad v_{\rm Hill} = \Omega r_{\rm Hill} \tag{195}$$

which gives an effective cross-section $\tilde{\sigma}$ for planetesimal–planetesimal encounters. Equation (193) reduces to the well-known gravitational focusing formula in the limit of high velocities:

$$\tilde{\sigma} \propto \sigma_{\rm geom} \left(1 + \frac{v_\infty^2}{v_{\rm rel}^2}\right) \tag{196}$$

$$v_\infty^2 = \frac{2G(m_1 + m_2)}{R_1 + R_2}. \tag{197}$$

If the vertical velocity dispersion is small, the disc becomes two-dimensional and the cross-section is proportional to R. The main differences to the two-body cross-section in equation (196) is a finite gravitational focusing factor, since the Keplerian shear inhibits a zero relative velocity, and a finite collisional probability for very small velocities, again due to the shear which provides a finite influx of particles. At the low-velocity limit, our results compare with those of Goldreich, Lithwick & Sari (2004), which have been explored by N-body simulations.

The precise calculation of the coagulation kernel should include an integration over all semimajor axes with a proper weighting kernel. As collisions among particles in the statistical model play only a major role when the system is still homogenous, we omitted this contribution. In addition, this helps saving computational time, since the solution of the coagulation equation is very costly. However, interactions between N-body particles and the statistical model include spatial inhomogeneities properly (see Section 11).

10.11 Discretization

All involved quantities are only functions of a and m. Therefore, we introduce a two-dimensional grid, where Σ, T_r and T_z are cell-centred quantities. Fig. 10 summarizes the definition of the two-dimensional grid. Since the full planetesimal size range covers several orders of magnitude in mass, we chose a logarithmically equidistant discretization in mass to cover the necessary mass range in a reliable way. The radial spacing of the grid cells is equidistant.

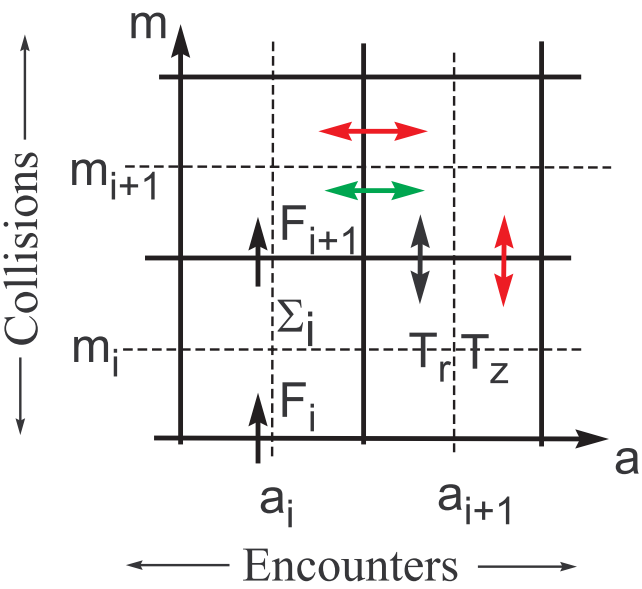

Figure 10. Numerical grid. The arrows indicate transport of kinetic energy (red), spatial transport of mass(green) and accretion (black). Non-neighbouring cells are coupled by the coagulation kernel and the radial interpolation kernel.

Thus, the grid setup for the mass discretization reads (N grid cells from $m_{\rm min} \ldots m_{\rm max}$):

$$m_i = m_{\rm min}\delta^{-i}(1/2 + \delta/2) \qquad i = 1, \ldots, N$$

$$\Delta m_i = m_{\rm min}\delta^{-i}(1 - \delta)$$

$$\Sigma_i = \frac{{\rm d}\Sigma}{{\rm d}m}\Delta m_i$$

$$\delta = \left(\frac{m_{\rm min}}{m_{\rm max}}\right)^{1/N}. \tag{198}$$

The grid spacing δ controls the number of cells which are necessary to cover a specified mass range. As the evaluation of the coagulation equation scales with the third power of the number of grid cells, δ should be as large as possible. If the flux integral is approximated in a standard way

$$F_i = -\sum_{j=1}^{N}\sum_{k=1}^{N} F_i^{(jk)}$$

$$F_i^{(jk)} = \frac{1}{\sqrt{2\pi(h_j^2 + h_k^2)}} \frac{\Sigma_j}{m_j}\frac{\Sigma_k}{m_k} \times \sigma(m_j, m_k)$$

$$\times\, v_{\rm rel} M_{\rm red}(m_i - \Delta m_i/2, m_j, m_k), \tag{199}$$

a spacing δ much smaller than 2 is required to guarantee a sufficient accuracy[20]. However, it is possible to use a spacing of 2 if special precaution is taken. Spaute et al. (1991) approximated the surface density with a power law, thus taking the gradient with respect to mass into account. While they reached only a sufficient accuracy with further special adaptations, we use a more rigorous approach. A large spacing δ reduces the accuracy, since the partial flux (equation 199) is strongly varying even inside one grid cell. Thus, we

[19] Their work includes an averaging over the Rayleigh distributed inclinations and eccentricities of the colliding planetesimals.

[20] Ohtsuki, Nakagawa & Nakazawa (1990) give a thorough analysis of the importance of the resolution.

Downloaded from http://mnras.oxfordjournals.org/ at MPI Gravitational Physics on January 13, 2015

rearrange this expression to identify the most important terms, as we can see in equation (200):

$$F_i^{(jk)} = \frac{v_{\rm rel}}{\sqrt{2\pi(h_j^2+h_k^2)}}\frac{\Sigma_k}{m_k}\underbrace{\frac{\Sigma_j}{m_j}\times\sigma(m_j,m_k)m_j}_{F_V(m_j)}\frac{1}{m_j}M_{\rm red} \times(m_i-\Delta m_i/2,m_j,m_k) \quad j\geq k. \tag{200}$$

The strongest varying contribution F_V is now approximated by a power law with respect to m_j:

$$F_V(m)\approx F_V(m_j)\left(\frac{m}{m_j}\right)^q. \tag{201}$$

Thus, equation (201) is used to provide improved partial fluxes $F_i^{(jk)}$ and thus we come to equation (202).

$$F_i^{(jk)} = \frac{v_{\rm rel}}{\sqrt{2\pi(h_j^2+h_k^2)}}\frac{\Sigma_k}{m_k} \times\int_{m_j-\Delta m_j/2}^{m_j+\Delta m_j/2}\frac{F_V(m)}{m\Delta m_j}M_{\rm red}(m_i-\Delta m_i/2,m,m_k)\,{\rm d}m \quad j\geq k. \tag{202}$$

Since the fragment redistribution function is a piecewise power law, an analytical solution of the integral is possible. Equation (202) gives reliable results even with a spacing $\delta=2$. The time derivative of the surface density reads

$$\dot{\Sigma}_m^i = -F_{i+1}+F_i \tag{203}$$

which should assure the conservation of mass within numerical accuracy.

We note that for calculations with a fixed mass grid (where the average mass of a bin is constant in time), $\delta<2$; otherwise, spurious solutions result (Ohtsuki et al. 1990). Other schemes use the approach of Wetherill (1989), the mass 'batches', where the average mass of a bin varies with time. In this case, δ can be any value. However, the latency between the actual time a particle reaches a specific size and the calculated time grows with δ. It has been noted that lags of a few per cent require $\delta\leq 1.25$ (Kenyon & Luu 1998). Nevertheless, a $\delta\sim 2$ yields lags of about 10 per cent, acceptable in view of the uncertainties in the whole approach.

10.12 Integrator

All contributions to the evolution of the surface density Σ and the velocity dispersions $T_{\rm r}$ and T_z are summarized by the following set of differential equations:

$$D = \frac{4}{3\Omega^2}\left(\frac{5}{4}\dot{T}_{\rm r,enc}+\dot{T}_{z,\rm enc}\right)$$

$$\frac{{\rm d}\Sigma}{{\rm d}t} = \Delta_a(D\Sigma)+\dot{\Sigma}_{\rm coll}$$

$$\frac{{\rm d}\Sigma T_{\rm r}}{{\rm d}t} = \Delta_a(D\Sigma T_{\rm r})+\Sigma\dot{T}_{\rm r}+\frac{\rm d}{{\rm d}t}(\Sigma T_{\rm r})_{\rm coll}$$

$$\frac{{\rm d}\Sigma T_z}{{\rm d}t} = \Delta_a(D\Sigma T_z)+\Sigma\dot{T}_z+\frac{\rm d}{{\rm d}t}(\Sigma T_z)_{\rm coll}. \tag{204}$$

The Laplace operator is approximated in accordance with the equidistant radial grid:

$$\Delta_a f = \frac{1}{a}\frac{\partial}{\partial a}\left(a\frac{\partial}{\partial a}f\right)$$

$$\Delta_a f \approx \frac{f_{i+1}(1+\Delta a/(2a_i))-2f_i+(1-\Delta a/(2a_i))f_{i-1}}{(\Delta a)^2}. \tag{205}$$

We chose the Heun method [21] as the basic integrator for the statistical model. It is a second-order accurate predictor–corrector scheme (X is a vector containing all the above quantities):

$$\frac{{\rm d}X}{{\rm d}t} = f(X)$$

$$X^p = X_n+\Delta t f(X_n)$$

$$X_{n+1} = X^p+\frac{1}{2}\Delta t(f(X^p)-f(X_n))+\mathcal{O}(\Delta t^3). \tag{206}$$

The Heun method is readily extended to an iterate scheme, which is equivalent to the implicit expression:

$$X_{n+1} = X_n+\frac{1}{2}\Delta t(f(X_{n+1})+f(X_n)). \tag{207}$$

This adds stability to the method and allows the secure integration of stiff configurations that may appear during the runaway accretion phase. In practice, three iterations are sufficient to guarantee a stable integration. As the diffusive part is discretized with a first-order accurate formula (see equation 205), the whole iterated scheme is equivalent to the Crank–Nicolsen method. We choose a global time step for the statistical model according to the expression

$$\Delta t = \min\left(\eta_{\rm Disc}\frac{X}{\dot{X}},X\in\{\Sigma,T_{\rm r},T_z\}\right), \tag{208}$$

where the hybrid code (see next section) applies an additional discretization in powers of two to achieve a better synchronization with the N-body code component.

Since we use the continuous form of the coagulation equation (see Sections 5 and 5.1), we also have 'half bodies'. In the mass regime of relevance, these are so copious that non-integer collision rates do not need to be treated with a random number generator. This is where the direct-summation N-body integrator of the scheme is relevant.

11 BRINGING THE TWO SCHEMES TOGETHER: THE HYBRID CODE

We introduced two different methods to solve the planetesimal growth problem. On the one hand, we modified NBODY6++, which has been used so far mainly for the simulation of stellar clusters, to adapt it to the special requirements of a long-term integration of planetesimal orbits. On the other hand, we developed a new statistical code with a consistent evolution of the velocity dispersion, the capability to treat spatial inhomogeneities and a thoroughly constructed collision treatment. Neither of the two approaches is powerful enough to provide a complete and accurate description of the planetesimal problem, since each method is confined to a certain range of the particle number. However, these restrictions are complementary in the sense that each method covers a regime

[21] The name of this method is not unique. Some texts denote it as the modified Euler method. The Heun method is a special case of the Runge–Kutta methods.

Downloaded from http://mnras.oxfordjournals.org/ at MPI Gravitational Physics on January 13, 2015

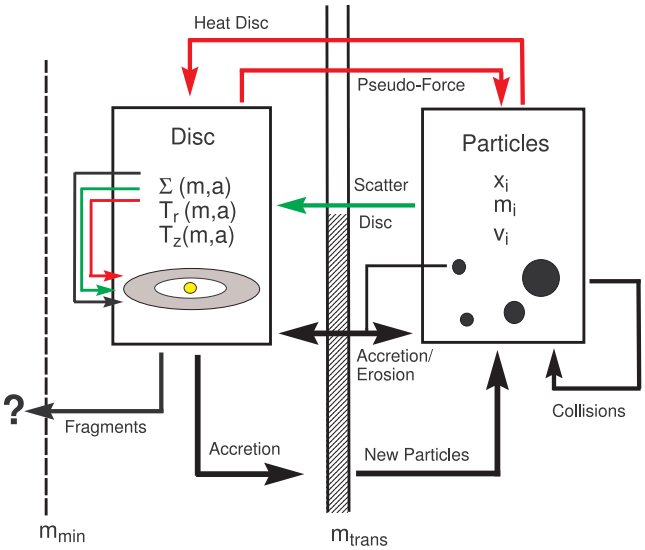

Figure 11. Interplay between the *N*-body component and the statistical component of the hybrid code. Black arrows indicate mass transfer, red arrows exchange of kinetic energy and green arrows indicate spatial structuring, respectively.

where the other method fails. This intriguing relation stimulated the construction of a hybrid code which combines the benefits of both methods.

The basic idea is to introduce a transition mass $m_{\rm trans}$, which separates the two mass regimes. Particles with a lower mass are treated by the statistical model, whereas larger particles belong to the *N*-body model. Though both parts are clearly divided in different mass ranges, they are connected by various interdependences.

(i) Direct collisions between particles lead to a mass exchange. One process is the accretion of small particles by *N*-body particles, but agglomeration within the statistical model can also produce particles larger than the transition mass. This requires the generation of new *N*-body particles. Energetic impacts may erode larger particles, so a corresponding particle removal is also required for consistency.

(ii) Mutual scatterings among *N*-body particles and smaller planetesimals transfer kinetic energy. While energy equipartition leads to a systematic heating of the smaller field planetesimals, a consistent treatment has to include both transfer directions.

(iii) Accretion and scattering by the *N*-body particles induce spatial inhomogeneities or even gaps in the planetesimal component, if the particles have grown massive enough. Likewise, the small particles could induce some structure in the distribution of the *N*-body particles. Since the spatial structure is dominated by the stirring from few protoplanets, we neglect the latter process.

Fig. 11 summarizes this brief overview of the interactions between the two code components in a schematic diagram. The following sections explain the implementation of each interaction term in more detail.

11.1 Mass transfer

An *N*-body particle accretes smaller particles in its vicinity. We already derived expressions which describe agglomeration within the statistical model, so it is manifest to apply these formulae to derive the accretion rate of an *N*-body particle.

Most of the material is accreted within the cross-sectional area σ (see equation 194), but the finite eccentricity of an orbit extends the accessible radial feeding zone. Thus, we assign the following surface density to each particle

$$\Sigma(a) = \frac{M}{2\pi a\sqrt{2\pi}l}\exp\left(-\frac{(a-a_0)^2}{2l^2}\right) \tag{209}$$

$$l^2 = \sigma/\pi + \frac{1}{2}a^2e^2 + T_{\rm r}/\Omega^2 \tag{210}$$

by smearing it out over its feeding zone. $T_{\rm r}$ is the radial velocity dispersion of particles in the statistical model with semimajor axis a. This density distribution is projected on to the radial grid to calculate the accretion rate. As the time step of the statistical model is much larger than the regular step of an *N*-body particle, the particle mass update is synchronized with the statistical integration. The projection technique allows the calculation of the accretion rates in a simple way, which gives the right size of the feeding zone and the proper total accretion rate.

Particle generation is included in the following way: a 'virtual' mass bin is introduced as the boundary between the statistical grid (denoted by the dashed area in Fig. 11) and the *N*-body component. Its sole task is to store mass and kinetic energy that drives the statistical model towards higher masses. If the mass content exceeds one $m_{\rm trans}$, a new particle is created with inclination and eccentricity according to the stored velocity dispersions.

The masses of the *N*-body particles are regularly checked to detect any particle which dropped below the transition mass. While this procedure would remove the particle and transfer the associated quantities back to the grid, we never observed such a particle erosion.

11.2 Disc excitation

The projection of an *N*-body particle on to the grid with the help of a proper weight function is also useful for the calculation of the disc excitation due to stirring by the larger particles. Since the Hill radius sets the proper length-scale for planetesimal encounters, the weight function is modified to

$$\Sigma(a) = \frac{M}{2\pi a\sqrt{2\pi}l}\exp\left(-\frac{(a-a_0)^2}{2l^2}\right)$$

$$l^2 = R_{\rm Hill}^2 + \frac{1}{2}a^2e^2 + T_{\rm r}/\Omega^2, \tag{211}$$

where $T_{\rm r}$ is the radial velocity dispersion of the heated planetesimal component. The velocity dispersion of the stirring *N*-body particle is [in accordance with equations (4) and (5)]:

$$T_{\rm r,0} = \frac{1}{2}(\Omega a_0)^2e^2 T_{\rm z,0} = \frac{1}{2}(\Omega a_0)^2 i^2. \tag{212}$$

We employ the orbital elements as mediators between the fast varying instantaneous position and velocity of a particle and the slow evolution of the statistical model, which operates on a longer relaxation time-scale. In virtue of the projection of the particle, we readily apply the standard interaction terms (see Section 10) to evaluate the additional heating due to the presence of *N*-body particles.

11.3 Pseudo-force

While an *N*-body particle is moving through the disc, it also interacts gravitationally with the particles in the statistical model. The collective effect of all these encounters leads to a change in the orbital elements of the *N*-body particle. Again, we project the *N*-body

Downloaded from http://mnras.oxfordjournals.org/ at MPI Gravitational Physics on January 13, 2015

particle on to the grid and evaluate the stirring rates $\dot{T}_r$ and $\dot{T}_z$, which correspond to a change in the orbital elements:

$$\frac{\mathrm{d}}{\mathrm{d}t}e^2 = \frac{2\dot{T}_r}{(\Omega a_0)^2}$$

$$\frac{\mathrm{d}}{\mathrm{d}t}i^2 = \frac{2\dot{T}_z}{(\Omega a_0)^2}. \tag{213}$$

These time derivatives of eccentricity and inclination are translated to a pseudo-force that effects the desired change of the orbital elements. We chose the ansatz

$$\boldsymbol{F}_{x,y} = C_r(\boldsymbol{v}_{x,y} - (\boldsymbol{v}_K)_{x,y})$$

$$\boldsymbol{F}_z = C_z\boldsymbol{v}_z, \tag{214}$$

where $\boldsymbol{v}_K$ is the local Keplerian velocity. In addition, we tried a simpler expression

$$\boldsymbol{F}_{x,y} = 2C_r\boldsymbol{r}_{x,y}\frac{\boldsymbol{r}\cdot\boldsymbol{v}}{r^2}$$

$$\boldsymbol{F}_z = C_z\boldsymbol{v}_z \tag{215}$$

without any significant differences in the accuracy or the simulation outcome. The proper friction coefficients are

$$C_r = \frac{\dot{T}_r}{2T_r}$$

$$C_z = \frac{\dot{T}_z}{2T_z}. \tag{216}$$

Since the relevant quantities are the time derivatives of the orbital elements, any other pseudo-force is also applicable. Though this approach yields the right mean change of the orbital elements, it lacks the statistical fluctuations from the particle disc. Hence, the distribution of the orbital elements of the *N*-body particles is artificially narrowed, which is especially important when the *N*-body particles and the statistical particles have a comparable mass. As the mass contrast between the two code parts is quite significant in planet formation simulations, it is safe to neglect the fluctuating part without major restrictions on the realism of the simulations.

The friction coefficients C_i are kept constant between two integration steps of the statistical model. While a more frequent update of the coefficients would be easily possible, a regular update on the basis of the statistical time step is accurate enough. Moreover, each update poses a considerable computational effort (roughly equivalent to 1000 force evaluations), so our approach also saves valuable computational time.

11.4 Spatial structure

The first insight into planetesimal formation was obtained by the particle-in-a-box method, which invokes the underlying assumption that the planetesimal disc stays homogeneous throughout the protoplanet growth (see e.g. Greenberg et al. 1978). While few large bodies introduce some coarse-graininess of the surface density, all smaller bodies are assumed to be evenly spread in the disc. Research on the interaction of protoplanets showed that this is an oversimplification, as bodies that are massive enough could open gaps in their vicinity (see e.g. Lin & Papaloizou 1979; Rafikov 2001). Gap formation does not only change the overall surface density, but also controls the accretion on to the protoplanet through the amount of planetesimals in the feeding zone. If gap formation is too effective, the growth of the protoplanet may well stop before the isolation mass

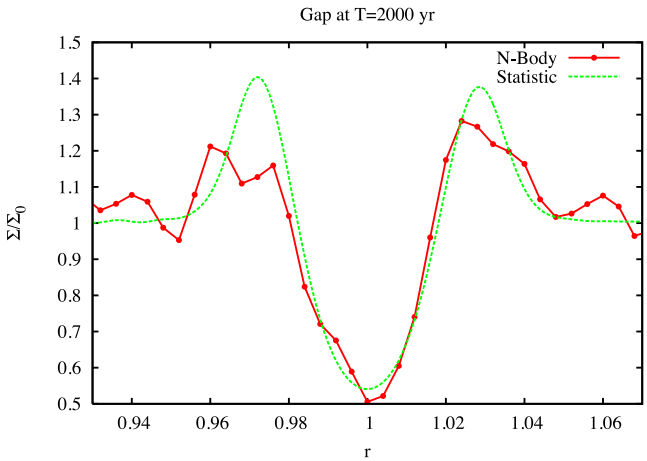

Figure 12. Gap opening in a planetesimal disc. The gap is fully developed after 2000 yr.

is reached. Hence, any hybrid code should provide a framework that allows this mechanism to operate. A necessary condition is a radial density grid with a sufficient resolution to describe possibly emerging gaps. A too low resolution suppresses local perturbations from the protoplanets by a simple averaging, thus inhibiting the formation of any spatial inhomogeneities. A second requirement is that the interaction terms relating statistical model and *N*-body model include the local interaction between particles and the statistical component in a proper way.

Our hybrid approach includes gap formation implicitly through the diffusive terms. A protoplanet heats only the planetesimals in its vicinity (defined by the heating kernel), thus also increasing locally the diffusion coefficient. Hence, the surface density drops due to outward diffusion of the planetesimals, given that the protoplanet is massive enough. The minimum gap opening mass is set by the condition that the protoplanet controls the random velocities of the field planetesimals in its heating zone (see equation 12), which is equivalent to the independently derived gap formation criterion (compare equation 14).

Although our algorithm invokes a simplified picture of the protoplanet–planetesimal interaction, it is surprisingly accurate with respect to the width of the forming gap and the opening criterion. Fig. 12 shows a simulation which examines the accuracy of our approach, and see Table 9 for a summary of the initial conditions for the comparative runs. The overall performance of the statistical code is quite remarkable, except a significant overestimation of the surface density at the gap boundary compared to the *N*-body model. This deviation is due to the improper treatment of strong planetesimal–protoplanet encounters, which exceed the diffusive approximation. Moreover, the higher concentration of planetesimals near the gap boundary leads to an additional overestimation of the velocity dispersion of the smaller planetesimals in the statistical calculation (see Fig. 13). While the comparison with the *N*-body calculation clearly indicates a necessary improvement of the treatment of spatial inhomogeneities, our approach catches the main features of gap formation.

11.5 Transition mass

Since the inventory of the new hybrid code is now completed, we turn to the specification of the transition mass m_{trans}. The mass boundary between statistical and *N*-body part has a major influence

Downloaded from http://mnras.oxfordjournals.org/ at MPI Gravitational Physics on January 13, 2015

Table 9. Parameters of the statistical and the *N*-body gap simulation. The perturber is placed at the centre of the ring.

No.	Σ	Δa	N	$N_{\rm rad}$	e^2/h^2	i^2/h^2	m	Type
G1	1.1251×10^{-6}	0.2	1406	–	0.001 35	0.001 35	1×10^{-9}	*N*-body
	Perturber	–	1	–	$e = 6.1 \times 10^{-5}$	$i = 3.2 \times 10^{-5}$	1×10^{-7}	–
G2	1.1251×10^{-6}	0.2	–	201	0.001 35	0.001 35	1×10^{-9}	Statistic
	Perturber	–	1	–	$e = 6.1 \times 10^{-5}$	$i = 3.2 \times 10^{-5}$	1×10^{-7}	–

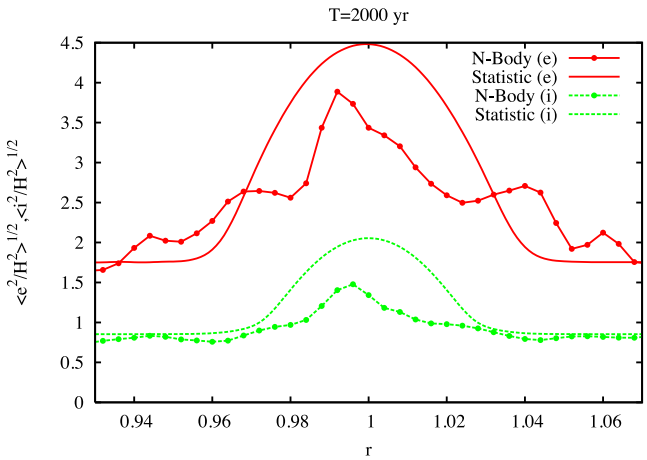

Figure 13. Mean square eccentricity and inclination of the smaller planetesimals in terms of the reduced Hill radius H of the protoplanet according to simulation G1 (*N*-body) and G2 (Statistic).

on the realism and the speed of the simulation. On the one hand, optimization with respect to speed favours a large transition mass, whereas a reasonable resolution of the transition between the two components introduces some upper limit.

Hence, we identify first the set of large masses, which controls the velocity dispersion of the disc, since these objects are also possible candidates for gap opening. The inspection of all involved stirring terms gives approximately the inequality:

$$\int_0^{m_{\rm trans}} \frac{{\rm d}\Sigma}{{\rm d}m} m \, {\rm d}m < \int_{m_{\rm trans}}^{\infty} \frac{{\rm d}\Sigma}{{\rm d}m} m \, {\rm d}m. \tag{217}$$

While this is a necessary condition to select all potential major perturbers, criterion (217) does not imply that all particles in the selected mass range exert indeed a strong influence on the disc. The number of possible gaps – and therefore the number of perturbers associated with them – is ultimately limited by the available space. Thus, we integrate the area of all potential gaps (width $\approx f_\Delta R_{\rm Hill}$) and normalize it to the total disc area:

$$f_{\rm C} \approx \int_{m_{\rm trans}}^{\infty} f_\Delta \frac{{\rm d}\Sigma}{{\rm d}m} \frac{2\pi a R_{\rm Hill}}{m} {\rm d}m. \tag{218}$$

If the covered fraction $f_{\rm C}$ is much larger than one, it is possible to increase the transition mass until the condition

$$f_{\rm C} \lessapprox 1 \tag{219}$$

is fulfilled. Of course, conditions (217) and (219) defined only an upper limit of the transition mass, so the adaptation of a lower value is also possible. Though there are two reliable conditions at hand, the transition mass is still a function of time owing to the time evolution of the density $\Sigma(m)$. Therefore, we chose a priori a fiducial value of the transition mass, run the simulation and conduct an a posteriori check, whether the initial choice matches our requirements at any evolutionary stage of the disc. A reliable value for a Solar system analogue at 1 au is

$$m_{\rm trans} \approx 3 \times 10^{-11}\,{\rm M}_\odot \tag{220}$$

which restricts the number of *N*-body particles to a tractable amount. Later stages would allow an even larger transition mass, but the current hybrid code does not include any dynamical adjustment of the transition mass at runtime.

11.6 Boundary conditions

Any numerical simulation is limited to a finite simulation volume and a finite time interval. Therefore, it is mandatory to introduce proper boundary conditions which provide a reasonable closure of the simulation volume.

While boundary conditions with respect to time are the familiar initial conditions, the choice of the spatial boundary conditions for the various involved quantities depends on the problem at hand and the type of the boundary. A simulation boundary can be due to physical reasons (like walls of a concert hall, surface of a terrestrial planet) or simply due to a limitation in computational power that inhibits the complete numerical coverage of the problem.

The current capability of the hybrid code sets limits on the radial range as well as on the covered mass range, which a simulation can handle in a reasonable time. Hence, we have to introduce artificial boundaries in radius, and a lower limit for the mass grid.

Any migration process couples the evolution of a local ring area in the planetesimal disc to the evolution of the whole disc. Inward (or outward) migrating material also transports information on the radial zone where the material originated from. As this information is not available within the frame of a local simulation, any choice of the boundary condition alters the evolution to some extent.

However, we focus on a formation stage where migration is not a dominant process, but provides only removal of the smaller collisional fragments. Thus, we apply closed boundary conditions for the outer and inner radius of the ring area (i.e. all fluxes vanish at the boundary), and an open boundary for the lower end of the mass range. While these conditions exclude the study of migrational processes, we gain clearer insight into the protoplanet growth.

12 DISCUSSION AND CONCLUSIONS

The formation of planetary systems represents a challenge from a numerical standpoint. The dynamical problem spans over many orders of magnitudes in length and demands the combination of different techniques. We have presented a composite algorithm that brings together the advantages of direct-summation tools and statistics for the description of the planetesimal disc. Direct-summation *N*-body techniques have been around for some decades and have proven their accuracy in a very large number of studies of stellar

Downloaded from http://mnras.oxfordjournals.org/ at MPI Gravitational Physics on January 13, 2015

clusters such as galactic nuclei and globular and open clusters. We deem it to be the numerical tool to integrate the motion of the bodies for the very precise integration of the orbits and treatment of close encounters. Typically, in a simulation of a stellar system, the energy is conserved in each time step by $E/\Delta E \sim 10^{-11}$ (where E is the total energy and ΔE the difference between the former and current total energy for a specific time), so that even if we integrate for a long time the cluster, the accumulated energy error is negligible. Nevertheless, porting the numerical tool to the problem of planetary dynamics is not straightforward and requires important modifications and additions. In this work, we present them in detail: the neighbour radius selection for the protoplanets, the Hermite iteration and we introduce for the very first time the new extended Hermite scheme, since the usual Hermite scheme is not sufficient to integrate planetesimal orbits accurately enough. Then, we bring in new forces to the problem, namely the introduction of the central potential of the star, as well as the drag forces, which depend on the gas density and size of the planetesimals. Hence, the regularization scheme, crucial to exactly integrate the close encounters, has to be accordingly modified. We then introduce the disc geometry and discuss the required changes to the neighbour scheme and prediction, as well as the communication algorithm and block size distribution.

For the statistical description of the planetesimal disc, we employ a Fokker–Planck approach. We include dynamical friction, high- and low-speed encounters, the role of distant encounters as well as gas and collisional damping and then generalize the model to inhomogenous discs. We then describe the combination of the two techniques to address the whole problem of planetesimal dynamics in a realistic way via a transition mass to integrate the evolution of the particles according to their masses.

In particular, we introduce and describe the extended Hermite scheme, which reduces the energy error by three orders of magnitude with the same number of force evaluations, compared to the standard version of NBODY6++.

While the implementation and some code details are newly introduced to the field of planet formation simulations, the first hybrid approach was developed in the early 1990's. Spaute et al. (1991, further improved in Weidenschilling et al. 1997) constructed a hybrid code with a statistical component to treat the smaller particles and a special treatment for the larger particles. A statistical model covers the field planetesimals with the help of a distribution function (similar to Wetherill 1989), whereas the larger particles are individually stored and characterized by mass, semimajor axis, eccentricity and inclination. While the interaction between these single particles and the statistical component is expressed by standard viscous stirring and dynamical friction terms, perturbations among the single particles are equated in a different way. First, the probability of an encounter of two neighbouring particles is calculated. This probability is used in a second step to decide whether a (numerically integrated) two-body encounter of the neighbouring particles is carried out to derive the change in the orbital elements. Though these two well-defined code components justify to speak about a hybrid approach, the Monte Carlo like integration of the largest particles is still closely related to a statistical treatment.

A modified *N*-body approach is used in the work of Levison & Morbidelli (2007). Their method covers the largest particles by a direct *N*-body code, which includes the smaller particles as 'tracer' particles. The term 'tracer' indicates that each particle represents a whole ensemble of planetesimals. In a similar line of approach and inspired by this idea, Levison, Thommes & Duncan (2010) modified a symplectic algorithm, SYMBA, to study the formation of giant planet cores. However, they made some assumptions in order to calculate the gravitational interaction between the planetesimals. In particular, they ignored totally close encounters between planetesimals (but see Levison, Duncan & Thommes 2012, for an update built on SYMBA), although they use their code in situations where interactions between planetesimals are small.

Ormel & Spaans (2008) present in their work a scheme based on Monte Carlo techniques to cover the vast range of sizes. For this, they assign more resolution to those particles that are more relevant to the interactions, typically the largest bodies. Smaller particles are grouped and treated collectively, which means that they all share the same mass and structural parameters. This classification is done in accordance to the 'zoom factor', a free parameter. Later, Ormel, Dullemond & Spaans (2010a) presented an detailed comparison of their Monte Carlo code with other techniques, in particular with pure direct-summation *N*-body results and other statistical studies and found that system leaves the runaway at a larger radius, in particular at the outer disc. With their simulations, the authors propose a new criterion for the runaway growth-oligarchy transition: from several hundreds of km in the inner disc regions up to a thousand km for the outer disc (Ormel, Dullemond & Spaans 2010b).

Bromley & Kenyon (2006) published a description of a hybrid method with a basic approach similar to our work. They employ two velocity dispersions and the surface density of the planetesimals to describe the planetesimal system. The statistical component includes migration of the planetesimals and dust particles due to gas drag and Pointing–Robertson drag. In contrast to our approach, they did not include mass transport due to the diffusion of the planetesimals, which precludes the study of spatial structures induced by the protoplanets. This issue was addressed later in their later work of Bromley & Kenyon (2011a,b), in which planets open up gaps in discs. One must note also that their method uses the standard discretization of the collisional flux (see equation 199) and thus restrict the spacing factor to $\delta \lesssim 1.25$ (Kenyon & Luu 1998). Bromley & Kenyon (2006) chose a set of test calculations which focused less on the technical aspects of their method, but on an overall comparison with a selected set of standard works on planet formation. Their test simulations are in good agreement with the references simulations, thus indicating a comparable quality of the method. Four years later, the authors presented an updated version of their code for planet formation. The new characteristics of the code included 1D evolution of the viscous disc, gas accretion on to massive cores, as well as accretion of small particles in planetary atmospheres (Bromley & Kenyon 2011a).

While a variety of hybrid approaches emerged over the past years, this technique is still far from a routinely application and is still challenged by many open issues. Hybrid codes bear the potential to address the dynamical evolution of a whole planetary system, the later stages of protoplanet formation initiate a strong interaction with the gaseous disc, which may require more diligence than the inclusion of a few additional interaction terms. However, the development is picking up speed, which places our work in a good position for further research.

ACKNOWLEDGEMENTS

PAS thanks the referee, Scott Kenyon, for his patience and time on a detailed and helpful refereeing of the paper. It is a pleasure to thank Sverre Aarseth, Cornelis Dullemond and Phil Armitage for comments on the manuscript. PAS thanks the National Astronomical Observatories of China, the Chinese Academy of Sciences and the Kavli Institute for Astronomy and Astrophysics in Beijing, for an extended visit, as well as the Aspen Center of Physics and the

Downloaded from http://mnras.oxfordjournals.org/ at MPI Gravitational Physics on January 13, 2015

organizers of the summer meeting, where this work was finished. PAS expresses his utmost gratitude to Hong Qi, Wenhua Ju and Xian Chen for their hospitality during his stay in Beijing and to the Kavli Institute for Theoretical Physics where one part of this work has been completed. This research was supported in part by the National Science Foundation under Grant No. NSF PHY11-25915 and supported by the Transregio 7 'Gravitational Wave Astronomy', financed by the Deutsche Forschungsgemeinschaft DFG (German Research Foundation). PG and RS acknowledge support by the Collaborative Research Group FOR 759 (Project C3) of German Science Foundation (DFG) 'The formation of Planets: The Critical First Growth Phase'. RS acknowledges support by the Chinese Academy of Sciences Visiting Professorship for Senior International Scientists, Grant Number 2009S1-5 (The Silk Road Project). The special supercomputer Laohu at the High Performance Computing Center at National Astronomical Observatories, funded by Ministry of Finance under the grant ZDYZ2008-2, has been used. Simulations were also performed on the GRACE supercomputer (grants I/80 041-043 and I/84 678-680 of the Volkswagen Foundation and 823.219-439/30 and /36 of the Ministry of Science, Research and the Arts of Baden-urttemberg). Computing time on the IBM Jump Supercomputer at FZ Jülich is acknowledged. PAS and RS thank the Aspen Center for Physics and the NSF Grant #1066293 for hospitality while part of the work for this paper was done.

REFERENCES

Aarseth S., 1999, PASP, 111, 1333
Aarseth S., 2003, Gravitational N-Body Simulations. Cambridge Univ. Press, Cambridge
Adachi I., Hayashi C., Nakazawa K., 1976, Prog. Theor. Phys., 56, 1756
Ahmad A., Cohen L., 1973, J. Comput. Phys., 12, 389
Andrews S. M., Rosenfeld K. A., Kraus A. L., Wilner D. J., 2013, ApJ, 771, 129
Armitage P. J., 2011, ARA&A, 49, 195
Astakhov S., Lee E., Farrelly D., 2005, MNRAS, 360, 401
Bagatin A., Cellino A., Davis D., Farinella P., Paolicchi P., 1994, Planet. Space Sci., 42, 1079
Balbus S., Hawley J., 1998, Rev. Mod. Phys., 70, 1
Balbus S., 2003, ARA&A, 41, 555
Bateman H., 1915, Mon. Weather Rev., 43, 163
Beauge C., Aarseth S. J., 1990, MNRAS, 245, 30
Beckwith S., 1996, Nature, 383, 139
Belyaev M. A., Rafikov R. R., 2011, Icarus, 214, 179
Benz W., Asphaug E., 1999, Icarus, 142, 5
Binney J., 1977, MNRAS, 181, 735
Binney J., Tremaine S., 2008, Galactic Dynamics: Second Edition, Princeton Univ. Press, Princeton, NJ
Blum J., Wurm G., 2000, Icarus, 143, 138
Bromley B. C., Kenyon S. J., 2006, AJ, 131, 2737
Bromley B. C., Kenyon S. J., 2011a, ApJ, 731, 101
Bromley B. C., Kenyon S. J., 2011b, ApJ, 735, 29
Burgers J., 1948, Adv. Appl. Mech., 1, 171
Cameron A. G. W., 1973, Space Sci. Rev., 15, 121
Cazenave A., Lago B., Dominh K., 1982, Icarus, 51, 133
Chandrasekhar S., 1942, ApJ, 97, 255
Connaughton C., Rajesh R., Zaboronski O., 2004, Phys. Rev. E, 69, 061114
Dohnanyi J., 1969, J. Geophys. Res., 74, 2531
Glaschke P., 2003, in Fridlund M., Henning T., Lacoste H., eds, ESA Special Publ., Vol. 539, Earths: DARWIN/TPF and the Search for Extrasolar Terrestrial Planets. ESA, Noordwijk, p. 425
Goldreich P., Tremaine S. D., 1978, Icarus, 34, 227
Goldreich P., Ward W. R., 1973, ApJ, 183, 1051
Goldreich P., Lithwick Y., Sari R., 2004, ApJ, 614, 497
Greenberg R., 1991, Icarus, 94, 98
Greenberg R., Hartmann W., Chapman C., Wacker J., 1978, Icarus, 35, 1
Greenzweig Y., 1992, Icarus, 100, 440
Hasegawa M., 1990, A&A, 227, 619
Hayashi C., 1981, Prog. Theor. Phys. Suppl., 70, 35
Hernquist L., Hut P., Makino J., 1993, ApJ, 402, L85
Hornung P., Pellat R., Barge P., 1985, Icarus, 64, 295
Housen K. R., Holsapple K. A., 1990, Icarus, 84, 226
Ida S., 1992, Icarus, 96, 107
Ida S., 1993, Icarus, 106, 210
Ida S., Kokubo E., Makino J., 1993, MNRAS, 263, 875
Inaba S., Barge P., Daniel E., Guillard H., 2005, A&A, 431, 365
Johansen A., Klahr H., Henning T., 2006, ApJ, 636, 1121
Johansen A., Oishi J. S., Mac Low M.-M., Klahr H., Henning T., Youdin A., 2007, Nature, 448, 1022
Kary D., Lissauer J., Greenzweig Y., 1993, Icarus, 106, 288
Kempf S., Pfalzner S., Henning T. K., 1999, Icarus, 141, 388
Kenyon S. J., Bromley B. C., 2004, AJ, 127, 513
Kenyon S. J., Luu J. X., 1998, AJ, 115, 2136
Kobayashi H., Tanaka H., Krivov A. V., Inaba S., 2010, Icarus, 209, 836
Kokubo E., 1996, Icarus, 123, 180
Kokubo E., 1997, Icarus, 131, 171
Kokubo E., Ida S., 2000, Icarus, 143, 15
Kokubo E., Yoshinaga K., Makino J., 1998, MNRAS, 297, 1067
Larson R., 1970, MNRAS, 147, 323
Leinhardt Z. M., Stewart S. T., 2012, ApJ, 745, 79
Levison H., Morbidelli A., 2007, Icarus, 189, 196
Levison H. F., Thommes E., Duncan M. J., 2010, AJ, 139, 1297
Levison H. F., Duncan M. J., Thommes E., 2012, AJ, 144, 119
Lin D., Papaloizou J., 1979, MNRAS, 188, 191
Lodders K., 2003, ApJ, 591, 1220
Makino J., 1988, ApJS, 68, 833
Mikkola S., Aarseth S. J., 1998, New Astron., 3, 309
O'Brien D., 2003, Icarus, 164, 334
O'dell C., Wen Z., Hu X., 1993, ApJ, 410, 696
Ohtsuki K., Nakagawa Y., Nakazawa K., 1990, Icarus, 83, 205
Ohtsuki K., Stewart G., Ida S., 2002, Icarus, 155, 436
Ormel C. W., Spaans M., 2008, ApJ, 684, 1291
Ormel C. W., Dullemond C. P., Spaans M., 2010a, ApJ, 714, L103
Ormel C. W., Dullemond C. P., Spaans M., 2010b, Icarus, 210, 507
Paszun D., Dominik C., 2009, A&A, 507, 1023
Petit J.-M., 1986, Icarus, 66, 536
Pinte C., Laibe G., 2014, A&A, 565, A129
Plummer H. C., 1911, MNRAS, 71, 460
Rafikov R., 2001, AJ, 122, 2713
Reipurth B., Jewitt D., Keil K. E., 2007, Lunar Planet. Inf. Bull., 110, 25
Safronov V. S., 1972, Evolution of the Protoplanetary Cloud and Formation of the Earth and Planets. Keter publishing House, p. 212
Schneider J., Amaro-Seoane P., Spurzem R., 2011, MNRAS, 410, 432
Shu F. H., Tremaine S., Adams F. C., Ruden S. P., 1990, ApJ, 358, 495
Spaute D., Weidenschilling S., Davis D., Marzani F., 1991, Icarus, 92, 147
Spurzem R., 1999, J. Comput. Appl. Math., Spec. Vol. Comput. Astrophys., 109, 407
Stewart G. R., Ida S., 2000, Icarus, 143, 28
Tanaka H., Inaba S., Nakazawa K., 1996, Icarus, 123, 450
Wada K., Tanaka H., Suyama T., Kimura H., Yamamoto T., 2009, ApJ, 702, 1490
Weidenschilling S. J., 1977, MNRAS, 180, 57
Weidenschilling S., Spaute D., Davis D., Marzari F., Ohtsuki K., 1997, Icarus, 128, 429
Wetherill G., 1989, Icarus, 77, 330
Wetherill G. W., Stewart G. R., 1993, Icarus, 106, 190
Youdin A. N., Chiang E. I., 2004, ApJ, 601, 1109

Downloaded from http://mnras.oxfordjournals.org/ at MPI Gravitational Physics on January 13, 2015

APPENDIX A: CENTRAL FORCE-DERIVATIVES

Central force $\boldsymbol{F}$ per mass (i.e. acceleration) and its time derivatives are

$$\begin{aligned}
\boldsymbol{F} &= -\frac{\boldsymbol{x}M}{x^3}\\
\boldsymbol{F}^{(1)} &= -\frac{\boldsymbol{v}M}{x^3} - 3A\boldsymbol{F}\\
\boldsymbol{F}^{(2)} &= -\frac{\boldsymbol{a}M}{x^3} - 6A\dot{\boldsymbol{F}} - 3B\boldsymbol{F}\\
\boldsymbol{F}^{(3)} &= -\frac{\dot{\boldsymbol{a}}M}{x^3} - 9A\boldsymbol{F}^{(2)} - 9B\boldsymbol{F}^{(1)} - 3C\boldsymbol{F}\\
\boldsymbol{a} &= \dot{\boldsymbol{v}}\\
A &= \frac{\boldsymbol{x}\cdot\boldsymbol{v}}{x^2}\\
B &= \frac{v^2}{x^2} + \frac{\boldsymbol{x}\cdot\boldsymbol{a}}{x^2} + A^2 = \dot{A} + 3A^2\\
C &= \frac{3\boldsymbol{v}\cdot\boldsymbol{a}}{x^2} + \frac{\boldsymbol{x}\cdot\dot{\boldsymbol{a}}}{x^2} + A(3B - 4A^2).
\end{aligned} \tag{A1}$$

The $\boldsymbol{F}^{(i)}$ denote the central force and its time derivatives, whereas $\boldsymbol{a}$ and $\dot{\boldsymbol{a}}$ refer to the total acceleration of the particle. The assumption that $\boldsymbol{x}$, $\boldsymbol{v}$, $\boldsymbol{a}$ and $\dot{\boldsymbol{a}}$ are independent of each other allows the derivation of averaged expressions for particle–particle interactions:

$$\begin{aligned}
\langle(\boldsymbol{F})^2\rangle &= m^2\frac{1}{x^4}\\
\langle(\boldsymbol{F}^{(1)})^2\rangle &= m^2\frac{2v^2}{x^6}\\
\langle(\boldsymbol{F}^{(2)})^2\rangle &= m^2\left(12\frac{v^4}{x^8} + 2\frac{a^2}{x^6}\right)\\
\langle(\boldsymbol{F}^{(3)})^2\rangle &= m^2\left(144\frac{v^6}{x^{10}} + 126\frac{a^2v^2}{x^8} + 2\frac{\dot{a}^2}{x^6}\right).
\end{aligned} \tag{A2}$$

We combine these expressions with Aarseth's time step formula to derive the regular time step as a function of the neighbour sphere radius R_s:

$$\begin{aligned}
\Delta t_\mathrm{reg} &\approx \sqrt{\eta_\mathrm{reg}}\frac{R_\mathrm{s}}{\bar{v}}\frac{1}{1+\sqrt{R_\mathrm{s}/R_0}}\\
R_0 &= 4\frac{\bar{v}^2}{a} \approx \frac{4\bar{v}^2\bar{r}^2}{Gm} = 4\frac{\bar{r}^2}{r_\mathrm{close}},
\end{aligned} \tag{A3}$$

where $\bar{r}$ is the average particle distance and r_close is the impact parameter for a 90-degree deflection.

APPENDIX B: SCALABLE COLLISIONS FLUX

The mass flux according to the perturbation equation (125) is

$$\begin{aligned}
F_\mathrm{p} &= -\iint(n(m_2)\Delta n(m_1) + n(m_1)\Delta n(m_2))\\
&\quad\times\sigma(m_1)v(m_2)m_1 f_m(m_1/m,\epsilon)\mathrm{d}m_1\mathrm{d}m_2\\
&= F^{(1)} + F^{(2)}.
\end{aligned} \tag{B1}$$

First, we employ the substitution

$$\begin{aligned}
m_1 &= mx_1\\
m_2 &= m_0\left(\frac{m_1}{m_0}\right)^{\frac{1+\alpha}{1+2w}}\left(\tilde{S}\right)^{\frac{1}{1+2w}}\epsilon^{\frac{1}{1+2w}}
\end{aligned} \tag{B2}$$

to solve for the partial flux $F^{(1)}$:

$$\begin{aligned}
F^{(1)} &= -n_0^2m_0^3\sigma_0v_0\int g(mx_1)F_1(x_1)\,\mathrm{d}x_1\\
F_1(x_1) &= \tilde{S}^{-k'}\int\epsilon^{-\frac{w+s+3+\alpha}{2+\alpha+2w}}\frac{f_m(x_1,\epsilon)}{x_1(1+2w)}\mathrm{d}\epsilon.
\end{aligned} \tag{B3}$$

The second contribution $F^{(2)}$ requires a slightly different transformation:

$$\begin{aligned}
m_1 &= mx_1\epsilon^{-1/(1+\alpha)}\\
m_2 &= m_0\left(\frac{mx_1}{m_0}\right)^{\frac{1+\alpha}{1+2w}}\left(\tilde{S}\right)^{\frac{1}{1+2w}}.
\end{aligned} \tag{B4}$$

Thus, the partial flux $F^{(2)}$ is

$$\begin{aligned}
F^{(2)} &= -n_0^2m_0^3\sigma_0v_0\int g(m_2)F_2(x_1)\,\mathrm{d}x_1\\
F_2(x_1) &= \tilde{S}^{-k'}\int\epsilon^{-\frac{w+s+3+\alpha}{2+\alpha+2w}}\frac{f_m(x_1\epsilon^{-1/(1+\alpha)},\epsilon)}{x_1(1+2w)}\mathrm{d}\epsilon.
\end{aligned} \tag{B5}$$

We change to a new set of logarithmic coordinates

$$u = \ln(m/m_0) \qquad u_1 = \ln(x_1) \qquad \tilde{s} = \frac{\ln(\tilde{S})}{1+\alpha} \tag{B6}$$

which transforms the total flux F_m to a convolution integral:

$$\begin{aligned}
F_\mathrm{p} &= -n_0^2m_0^3\sigma_0v_0\int[g(u+u_1)G_1(u_1)\\
&\quad + g\left(p(u+u_1+s_1)\right)G_2(u_1)]\,\mathrm{d}u_1
\end{aligned} \tag{B7}$$

$$p = \frac{1+\alpha}{1+2w}, \tag{B8}$$

where $p = 1$ refers to the already derived solution for self-similar collisions. Hence, we expand equation (B7) at $p = 1$ and retain only the zeroth-order moment of the fragmentation kernel:

$$F_\mathrm{p} = -n_0^2m_0^3\sigma_0v_0\left[g(u)G_{1,0} + \left(g(u) + u(p-1)\frac{\partial g}{\partial u}\right)G_{2,0}\right]. \tag{B9}$$

This expression is equivalent to

$$\begin{aligned}
F_\mathrm{p} &= -n_0^2m_0^3\sigma_0v_0(g(u)G_{1,0}\\
&\quad + [g(u) + (p-1)(g(u) - g(0))]G_{2,0}),
\end{aligned} \tag{B10}$$

where higher derivatives of $g(u)$ are neglected. Hence, we recover the same functional form of the perturbed mass flux F_p as for self-similar collisions:

$$\begin{aligned}
F_\mathrm{p} &= -n_0^2m_0^3\sigma_0v_0\,g(u)\left(G_{1,0} + p\,G_{2,0}\right) + \mathrm{const.}\\
&\quad\times\propto\tilde{S}^{-k'}.
\end{aligned} \tag{B11}$$

Downloaded from http://mnras.oxfordjournals.org/ at MPI Gravitational Physics on January 13, 2015

APPENDIX C: COAGULATION EQUATION

While the success of a general approximation of the coagulation equation depends heavily on the used coagulation kernel, we nevertheless provide a more general approach to embed Section 5 in a broader context. The standard coagulation equation is

$$0 = \frac{\partial}{\partial t} mn(t,m) + \frac{\partial}{\partial m} F_m(t,m)$$

$$F_m = -\iint n(t,m_1)n(t,m_2)\sigma(m_1,m_2) \times v_{\rm rel} M_{\rm red}(m,m_1,m_2)\,{\rm d}m_1{\rm d}m_2. \quad \text{(C1)}$$

In virtue of our experience drawn from the perturbation expansion, we transform the coagulation equation to logarithmic coordinates

$$u = \ln(m) \quad \text{(C2)}$$

and employ the size distribution $g(u)$ relative to the steady-state solution $n_{\rm eq}(m)$:

$$0 = \frac{\partial}{\partial t} g(u,t) n_{\rm eq}(u) {\rm e}^{2u} + \frac{\partial}{\partial u} F_u(t,m)$$

$$F_u = -\iint g(t,u_1)g(t,u_2)K(u,u_1,u_2)\,{\rm d}u_1\,{\rm d}u_2, \quad \text{(C3)}$$

where $K(u,\,u_1,\,u_2)$ is the properly transformed new coagulation kernel. $g(u)$ is expanded under the integral to arrive at a moment expansion of the flux F_u:

$$F_u = -K_{00}(u)g(u)^2 - (K_{10}(u) + K_{01}(u))g(u)\frac{\partial g}{\partial u} + \cdots$$

$$K_{ij} = \iint K(u,u_1,u_2)u_1^i u_2^j {\rm d}u_1{\rm d}u_2. \quad \text{(C4)}$$

Retaining only the leading-order terms, we recover an approximate coagulation equation which is similar to the inviscid Burgers' equation [22]:

$$0 = \frac{\partial}{\partial t} g(u,t) n_{\rm eq}(u){\rm e}^{2u} - \frac{\partial}{\partial u}\left(K_{00}(u)g(u)^2\right). \quad \text{(C5)}$$

[22] This notion goes back to Burgers (1948), but the equation was already introduced by Bateman (1915).

This paper has been typeset from a TEX/LATEX file prepared by the author.

Downloaded from http://mnras.oxfordjournals.org/ at MPI Gravitational Physics on January 13, 2015